

Modeling Pc4 Pulsations in Two and a Half Dimensions

DRAFT VERSION CREATED ON FEBRUARY 23, 2016

© Charles A McEachern 2016
ALL RIGHTS RESERVED

Acknowledgements

Acknowledgement placeholder.

Dedication

Dedication placeholder.

Abstract

Something something Pc4 pulsations. Ultra low frequency (ULF) waves with periods of a minute or two. They correspond to field line resonances near Earth's plasmapause. Drift or drift-bounce resonance with energetic radiation belt and ring current particles. Radial diffusion.

Pc4 pulsations are known to exhibit different behavior based on their azimuthal mode-number. Low- m Pc4 pulsations are driven at the outer edge of the magnetosphere, and have a compressional component. High- m Pc4 pulsations are non-compressional and are driven within the magnetosphere.

Giant pulsations are a subset of high- m Pc4 pulsations which are of particular interest. High- m Pc4 pulsations are hard to simulate. Traditionally, simulations are driven from the outer boundary, which doesn't work in this case. And resolving high azimuthal modenumbers is computationally expensive in a 3D simulation.

Chapter 1 gives a general introduction is made to Earth's magnetosphere. (Note: this doesn't exist yet.)

Chapter 2 summarizes Pc4 pulsations in terms of prominent theoretical and observational work, including work on giant pulsations. (Note: this mostly doesn't exist yet.) It also derives dispersion relations for a cold, resistive plasma, such as Earth's inner magnetosphere and ionosphere. This gives an idea as to the waves expected to be produced.

Chapter 3 presents a 2.5D model designed to simulate Pc4 pulsations, including those with high azimuthal modenumbers. The model is built upon recent work by Lysak, and includes a dipole-aligned geometry, a height-resolved ionosphere, and coupling to a conducting Earth. Ring current modulation is introduced as a novel driving mechanism.

Chapter 4 investigates the results of adding electron inertial effects to the model, allowing the computation of parallel electric fields and field-aligned currents.

Chapter 5 showcases changes in Pc4 behavior as a result of altering the azimuthal modenumber. This includes a rotation of poloidal to toroidal waves, significantly refining past work by Mann, and before that Radoski. (There are a lot of figures here. It might end up being two chapters.)

Chapter 6 compares model output to poloidal Pc4 observations made with the Van Allen Probes. (Note: this hasn't quite happened yet. The chapter briefly explains.)

Chapter 7 offers a summary and possibilities for future work.

NOTE: ALL FIGURES ARE PDFS. Some of the frames are small, but they should remain sharp when you zoom in on them.

Contents

Acknowledgements	i
Dedication	ii
Abstract	iii
List of Tables	viii
List of Figures	ix
1 The Near-Earth Environment	1
1.1 The Ionosphere	3
1.2 The Inner Magnetosphere	5
1.3 The Outer Magnetosphere	5
1.4 Geomagnetic Disturbances	6
2 Ultra Low Frequency Waves	7
2.1 Pc4 Pulsations	8
2.1.1 Giant Pulsations	8
2.2 Waves in Cold Resistive Plasmas	17
2.2.1 Parallel or Perpendicular Propagation	18
2.2.2 High Altitude Limit	20
2.2.3 Implications for This Work	21
3 Numerical Model	23

3.1	Coordinate System	25
3.1.1	Differential Geometry	26
3.1.2	Numerical Application	28
3.2	Maxwell's Equations	30
3.2.1	Linearization and Optimization	30
3.2.2	Magnetic Fields	31
3.2.3	Electric Fields	31
3.3	Driving	34
3.3.1	Outer Boundary Compression	34
3.3.2	Ring Current Modulation	36
3.4	Boundary Conditions	38
3.4.1	Inner and Outer Boundaries	38
3.4.2	Coupling to the Atmosphere	38
4	Electron Inertial Effects	42
4.1	Amending the Model	42
4.1.1	The Boris Approximation	43
4.2	Quantifying the Results	45
4.2.1	Parallel Electric Fields	45
4.2.2	Field-Aligned Current	48
4.2.3	Inertial Length Scales	50
5	Large Modenumber Effects	54
5.1	Finite Poloidal Lifetimes	54
5.1.1	High Conductivity	55
5.1.2	Low Conductivity	57
5.2	Spatial Distribution of Energy	59
5.2.1	Resonant Driving	61
5.2.2	Nonresonant Driving	63
5.3	Significance for Giant Pulsations	64
5.3.1	Ground Signatures	66
6	Comparison to Van Allen Probes	68

7 Conclusion	70
7.1 Summary of Results	70
7.2 Future Work	70
References	71
Appendix A. Differential Geometry	83
A.1 Glossary	83
A.2 Acronyms	83

List of Tables

1.1	Integrated Atmospheric Conductivity	4
1.2	Integrated Ionospheric Conductivity	5
2.1	IAGA Magnetic Pulsation Frequency Bands	7
A.1	Acronyms	83

List of Figures

1.1	Ionospheric Conductivity Profiles	4
2.1	Alfvén Speed Profiles	15
2.2	Alfvén Bounce Frequency Profiles	16
3.1	Nonorthogonal Dipole Grid	29
3.2	Decreasing Penetration with Increasing Modenumber	35
3.3	Sym-H Fourier Components for June 2013 Storm	37
4.1	Plasma Frequency Profile	45
4.2	Parallel Electric Field Snapshots	47
4.3	Field-Aligned Current and Poynting Flux at the Ionosphere	49
4.4	Ionospheric Power Density	50
4.5	Parallel Electric Fields by Perpendicular Grid Resolution	52
5.1	Poloidal and Toroidal Energy: Active Day	56
5.2	Poloidal and Toroidal Energy: Quiet Night	58
5.3	Poloidal and Toroidal Energy Distribution: Resonant Driving	61
5.4	Poloidal and Toroidal Energy Distribution: Nonresonant Driving	63
5.5	Dayside Ground Magnetic Fields	66

Chapter 1

The Near-Earth Environment

TODO: Sketch out the general structure of the magnetosphere, from the ionospheric current sheet (is this too generous?) to the magnetopause (a real current sheet). Talk about where gravity dominates, where field line curvature becomes apparent, and where the moon sits in all this.

One hundred kilometers above Earth's surface, more or less, the neutral atmosphere transitions sharply into the conducting ionosphere.

From [77]: "In the thermosphere, the solar ultraviolet (UV) light and energetic particles precipitating from the magnetosphere produce ionization increasing with altitude. At the same time the particle density is low enough to make the recombination times of the ionized atoms and molecules sufficiently long to allow a significant fraction of the gas to remain ionized. This produces a conducting layer of the atmosphere known as the ionosphere. The ionosphere begins at ~ 65 km, has a peak plasma density between 200 and 300 km, and eventually merges with magnetospheric regions $\sim 1000\text{--}2000$ km altitudes."

The ionospheric E region is collisionally coupled to the neutrals. This decouples the ion and electron drifts, allowing currents to flow perpendicular to the magnetic field.

300

1000

3000

10,000 (2RE geocentric)

30,000 (5 RE)

Moon is at 60 RE or so.

Tail goes back to about 100 RE.

Ionosphere is dense enough to be shaped by gravity, but as altitude increases, magnetic field dominates.

The nitrogen density (w at sea level) drops from x at 100km to y at 1000km to z at 10^{**4} km.

By 10^{**4} km, the curvature of Earth's dipole magnetic field becomes apparent... and, between the increasing ion abundance and the decreasing strength of gravity, it dominates particle behavior.

At 10^{**5} km, the bow shock. On the dayside, at least. Balance between Earth's magnetic field and that of the sun. Another current sheet... This one far more intense.

Still less than halfway to the moon. That's 3e5 km.

This all takes place well within the orbit of the moon. Moon is about 60 RE away

Where are satellites? Geosynchronous?

This with is concerned with the behavior of electromagnetic waves that propagate inside the magnetosheath, but outside the ionosphere; in fact, they play a significant role in the transport of energy from the former to the latter.

Free electron density...

Still mostly neutrals, but collisions are so rare that they don't matter. At x, the mean free path of a neutral atom is comparable to...

It's all about energy transfer! Sun generates energy through nuclear reactions. Some of this energy is transported in the solar wind, which drives behavior in the near-Earth environment.

At Earth's orbit, the solar magnetic field makes more-or-less a 45° angle with the X axis.¹

1.1 The Ionosphere

Pedersen, Hall, and field-aligned conductivity. Do we want to get into two-cell convection? Region 1 and 2 current?

TODO: Convection electric field. How close to Earth does it get? Don't we lose $\underline{E} = \underline{V} \times \underline{B}$ when there are currents?

"Increasing the Hall conductance allows the energy to oscillate through the inductive process rather than dissipate as Joule heating, increasing the 'ringtime' of field line resonances." [103]

Scale heights. Ion/neutral composition.

E, F layers.

Ionospheric Alfvén resonator. This is important if we want to talk briefly about all kinds of ULF waves.

Precipitation. Inverted V.

TODO: Scott's thesis has a TON of detail. How much does Jesse show?

¹Uppercase X , Y , and Z are used to indicate GSE coordinates: X points from the Earth to the Sun; Y is perpendicular to X in the Sun's ecliptic plane, pointing duskwards; Z points north, out of the ecliptic plane. In later chapters, lowercase x , y , and z are used to define a more-or-less analogous coordinate system with respect to Earth.

Pedersen (Blue), Hall (Red), and Parallel (Green) Conductivities

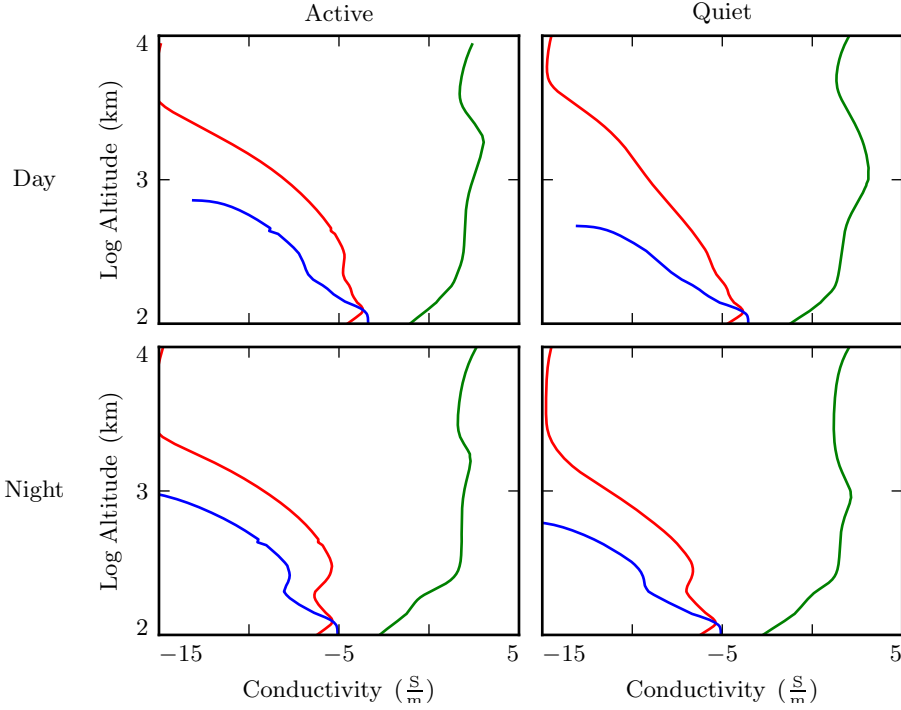


Figure 1.1: Ionospheric conductivity profiles, adapted by Lysak[65] from Appendix B of Kelley's textbook[48].

Table 1.1: Integrated Atmospheric Conductivity (S)

	Σ_0	Σ_P	Σ_H
Active Day	424	0.65	6.03
Quiet Day	284	0.44	4.02
Active Night	9	0.01	0.12
Quiet Night	9	0.01	0.12

Table 1.2: Integrated Ionospheric Conductivity (S)

	Σ_0	Σ_P	Σ_H
Active Day	—	13.0	17.0
Quiet Day	—	5.6	10.2
Active Night	—	0.8	0.3
Quiet Night	—	0.2	0.3

1.2 The Inner Magnetosphere

Closed field lines. More or less dipolar.

The plasmasphere and plasmapause.

Radiation belts. Radial diffusion is interesting because...

Alfvén speed. So we probably want to at least mention field line resonance here? Or do we get into that in the next chapter? Plot of Alfvén speeds and Alfvén bounce times for each profile.

1.3 The Outer Magnetosphere

Significant deformation by the solar wind.

Bow shock.

Magnetopause. Current sheet consistent with Ampère's Law.

Plasma sheet and PSBL.

Tail and tail lobes.

Reconnection.

1.4 Geomagnetic Disturbances

Storms! CMEs, etc.

What causes a storm.

Storm effects: outer magnetosphere, inner magnetosphere, on the ground.

The ionospheric profiles used in this model are based on values tabulated in the Appendix B of Kelley's book[48]. They were adapted by Lysak[65] to take into account the effect of the magnetosphere's latitude-dependent density profile.

Mean molecular mass of 28 u at 100 km, 16 u around 400 km, down to 1 u above 1400 km.

Simulations are carried out using four profiles: active day, quiet day, active night, quiet night.

Profiles are static for the duration of a simulation. Even so-called ultra low frequency waves are still much faster than convective timescales.

TODO: Come up with a characteristic convective timescale or two, and cite it.

The effects of mean molecular mass on conductivity are computed per the usual definitions.

$$\sigma_P = \sum_s \frac{n_s q_s^2}{m_s} \frac{\nu_s}{\nu_s^2 + \Omega_s^2} \quad \sigma_H = - \sum_s \frac{n_s q_s^2}{m_s} \frac{\Omega_s}{\nu_s^2 + \Omega_s^2} \quad \sigma_0 = \sum_s \frac{n_s q_s^2}{m_s \nu_s} \quad (1.1)$$

Each profile is resolved to an altitude of about 10^4 km, and include well-resolved E , F_1 , and F_2 layers.

Chapter 2

Ultra Low Frequency Waves

Pc1-2 are close to the proton cyclotron frequency.

Pc 3-5 are field line resonance.

Phenomenological. The boundaries are fuzzy since sometimes we want to talk about the underlying mechanisms.

Pi2: “Clearly linked to substorm disturbances and other impulsive dynamics are the irregularly shaped waves in the 7–25-mHz band referred to as Pi2. Recent work on these waves suggests that their periodicity reflects the spectrum of global mode excitations of the plasmasphere but there is a competing proposal that the dominant frequencies are imposed by the modulated flows in the magnetotail.”[50]

Table 2.1: IAGA Magnetic Pulsation Frequency Bands[45]

	Pc1	Pc2	Pc3	Pc4	Pc5	Pi1	Pi2
Period (s)	1–5	5–10	10–45	45–150	150–1000	1–20	20–1000
Frequency (mHz)	200–1000	100–200	22–100	7–22	1–7	25–1000	1–25

TODO: A few sentences about Pi1 pulsations. Frequency range, when/where they are seen, and why they are interesting.

TODO: Pi2.

TODO: Pc1.

TODO: Pc2.

TODO: Pc3.

TODO: Pc4.

TODO: Pc5.

2.1 Pc4 Pulsations

It seems like we should probably have a section called “Pc4 Pulsations” ... but won’t we mostly be talking about the idea of FLRs?

2.1.1 Giant Pulsations

“To summarize, the general buffetting of the magnetosphere by variations in the solar wind dynamic pressure, or perhaps by sporadic magnetic reconnection, provides a broad band energy source to the magnetosphere. The magnetospheric cavity as a whole rings at its own eigenfrequencies, thus transporting energy at just those frequencies to field lines deep in the magnetosphere. Those field lines whose eigenfrequencies match one of the cavity eigenfrequencies couple to the cavity mode and resonate strongly, producing the classical field line resonance signature.[42]”

Dungey’s Alfvén wave paper[19].

High-modenumber ULF pulsations are damped by the ionosphere, making it more difficult to observe them on the ground[43]. Small structures are also damped; resonances narrower than ~ 100 km aren’t visible on the ground.

TODO: See also Glassmeier and Stellmacher, 2000 (about small latitude), and Wright and Yeoman, 1999, Yeoman and Wright, 2001 about large m

Multi-spacecraft observation of a ULF wave with very high modenumber (70+) and no apparent ground signature[95].

A recent survey of Van Allen Probe data showed that Pc4 pulsations – the poloidal ones, at least – occur primarily during geomagnetically active times, near the plasmapause, over just a handful of hours of dayside MLT[13]. This confirmed and refined older work[24].

ULF waves have been shown to correlate with pulsating aurora and with chorus[46]. It's believed that (in the case presented) substorm injection drove Pc4-5 pulsations, which modulated chorus waves, which pitch-angle scattered electrons with energies on the order of 10 keV.

Energetic ring current and radiation belt particles can be accelerated by ULF waves through drift or drift-bounce resonance[89].

A Hall-conducting ionosphere reflects ULF waves[41].

"It is not clear why noncompressional [high- m] Pc4 poloidal waves, which are presumably driven by instability within the magnetosphere, preferentially occur on the dayside.[13]"

Poloidal and toroidal ULF polarizations are treated differently by the ionosphere[35] (or, more recently, [27]).

TODO: Theoretical consideration of decay vs propagation, by frequency. Lysak and Yoshikawa 2006.

TODO: Fishbone instability. McGuire 1983, Chen 1984. Similar phenomenon, but for lab plasmas.

An ideal poloidal mode decays to the toroidal mode in the presence of curved magnetic field lines[82] or a gradient in the Alfvén speed[69]. The time is proportional to the azimuthal wavenumber[69]. An analytical follow-up agreed with the numerical work[70].

TODO: Mann gives the poloidal-to-toroidal decay time to be $\tau = \frac{d\lambda}{d\omega'_A}$, where $\lambda = \frac{m}{2\pi r}$ and ω'_A is the spatial derivative of the Alfvén bounce frequency, but this doesn't seem to line up. When τ is computed using our Alfvén bounce frequencies, the result is much

less than 1 s. Double-checking is necessary.

Analysis of GOES data from 2008 to 2013 shows about 100 Pg events. They are concentrated on the morningside. No particular correlation with storm phase[71].

Recall compressional poloidal Pc4s are mostly during storm time, and noncompressional are mostly specifically during late recovery[13]. Only 19 fundamental poloidal mode examples were identified from the 390 noncompressional poloidal events.

Pgs are rare[6].

Most Pgs observed on the ground have m in the range 16 to 35[98].

Poloidal Pc4s may be caused by phase space gradients[14].

Fundamental standing waves are possibly excited by drift resonance of ions with energy around 100 keV[100, 14].

“It is unclear whether other generation mechanisms of fundamental standing waves such as drift wave instability[33] can explain the localization of Pgs in local time (LT).”[71]

Motoba[71] found m value in the range 10 to 15 for a sample of Pgs. Previous studies[84, 28, 40, 78] are in general agreement that Pg modenumbers fall into the range 16 to 35.

Another past study: [97]. Satellite data is surveyed and classified by polarization, harmonic, wavenumber, etc, in order to determine the mechanisms for generating Alfvén waves. Old, but still pretty representative, according to Motoba[71].

It seems to be the convention to find a Pg event on the ground, then look at satellite data. That’s certainly what was done in [71].

Per [71], most Pg events happen around $L = 7$, but some do happen near the plasma-pause, as seen(?) by [34].

“The AL distribution shown in Figure 14c are consistent with the findings of [84] that Pgs occur as the magnetosphere recovers from previous activities (substorms).”[71] Finds this to be reasonable because it’s “very likely” that energetic ions injected into the inner magnetosphere from the magnetotail provide energy to Pgs.

Second harmonic poloidal waves – as most of [13]’s events are – are unlikely to cause a Pg event on the ground[98].

[11]: Standing Alfvén waves in the magnetosphere. Theoretical fundamental toroidal and poloidal modes can vary by up to 30 % in frequency.

[71] suggests that Pgs originate from the fundamental poloidal mode waves at all local times.

First Pg observation[4].

Energetic particles can get accelerated (or deaccelerated) by the wave electric field through the drift or drift-bounce resonance[22].

Poloidal ULF waves are capable of energizing radiation belt electrons (not ions?) to very high energy through coherent drift/drift-bounce resonance interactions[22, 75, 68]. By multiple wave-particle interactions, poloidal ULF waves can lead to radial diffusion of radiation belt particles[21, 101, 76].

AMPTE/CCE data has shown a correlation between poloidal Pc4 activity and intense ring current flux near the equator[25].

Pc4 pulsations are radially localized, per multiple satellite observations[23], and spread no more than about 8 hours MLT. They peak around L of 5 to 6, with lower occurrence rate 2.5 to 9[2, 59].

Low m is compressional[42]. Drivers may include KH at the magnetopause[8, 88, 60], variations in solar wind pressure (such as interplanetary shocks)[109, 110, 38, 15, 49], and waves in the foreshock region[85, 92].

At high m , the poloidal mode decouples from the compressional mode[42] and becomes guided[11].

Most observed guided waves are second harmonic excited by the drift-bounce resonance[44, 87, 96]. Fundamental modes, driven by drift resonance, are rarer, but have been observed[14].

The plasmapause – representing a sharp change in Alfvén speed – is important for ULF waves. Waves are trapped and scattered by the effective potential well, analogous to

Schrödinger's equation[55, 56, 12]. This has been shown theoretically[51, 57, 52, 67] (most recent is [67]) and observationally[90, 91].

Because the inner magnetosphere is low- β (that is, magnetic pressure dominates thermal pressure), the strength of the compressional-poloidal coupling indicates m [42].

TODO: How so?

TODO: Haven't read this paper yet, but it looks fun: [31].

Pc5 waves peak around L of 7 to 9, too far out for RBSP[2, 59].

It's perhaps not surprising that, finding events based on ground signatures, m would skew low. High- m waves can't penetrate the ionosphere.

Compressional waves come from the outer boundary, propagating across field lines[62].

Compressional driving doesn't preclude drift or drift-bounce resonance[109, 110].

Plasmapause refilling may cause onset of the instability that drives noncompressional Pc4s[23, 58].

Note that Dai[13] was pretty generous about what counted as a storm... anything that hits -30 nT. So [71] may not have counted the same way when they found no particular correlation with storm phase.

Compressional poloidal Pc4 pulsations are much more common during storms, but not particularly sensitive to storm phase. Noncompressional ones occur primarily during recovery[13, 84, 23, 1].

In the example shown of a fundamental mode poloidal Pc4, and in the example of a higher harmonic Pc4, a mishmash of toroidal activity is present. [13], figure 8 and 9 respectively.

Poloidal Pc4 pulsations are common inside and outside the plasmapause. Plasmapause peaks at 4.8–5 RE and 5.8–6RE[13].

Drift resonance is the fundamental mode. Drift-bounce is higher harmonics[13].

TODO: Do the unambiguous Pc4 events in [94] and [14] also have a mishmash of toroidal activity?

Second harmonic: Br leads Ea by 90 degrees. Fundamental mode: Br lags Ea by 90 degrees. [13]

Low- m waves tend to be more muddled... driven by broadband sources rather than resonance[13].

Fundamental mode is rare. Of 390 noncompressional events, Dai identified 19 to be clearly fundamental mode and 197 to be clearly second harmonic[13].

TODO: Fishbone instability?

TODO: Lab Alfvén waves as LASP?

Fast and shear (toroidal and poloidal) modes are coupled by nonzero Hall conductivity[47].

Shear mode incident on the ionosphere, pederson current closes FAC, Hall current then generates a fast mode wave which may be detected in space or on the ground[99].

Toroidal mode is usually associated with external driving[8, 88].

Guided poloidal wave arises as m goes to infinity[80].

Observations show that the poloidal mode is most excited in the second harmonic[11, 44, 3, 87, 97, 25] even when there is a strong compressional component[93, 36, 102, 86].

Theoretical justifications for why the second harmonic would be preferentially excited in the ring current environment[89, 9, 10, 7].

The energy of the resonant particle gives m , recall $\omega - m\omega_d = 0$ or something[74].

Giant pulsations happen at large m , and do not produce ground signatures[95].

Observations of odd-mode poloidal waves... possible fundamental[107, 26].

Observations in space indicate that Pgs are fundamental poloidal mode[53, 40, 54, 98, 30].

Alfvén waves with small latitudinal scale[32] or high m [106, 108] are screened by the ionosphere. Attenuation factor from [43] and [29] DID NOT PRINT PROPERLY. LOOK IT UP.

Typical magnitude is order of a few nT, and a few mV/m[95].

Drift-wave instability[39, 33, 34] is also a possibility for exciting fundamental poloidal waves, though it requires cold plasma, so it could only happen in the plasmasphere.

Fundamental poloidal mode is drift resonance, not drift bounce[78].

Pgs are most common during solar minimum, perhaps because of decreased mass loading of heavy ions[16].

The Alfvén speed is computed from Kelley's low-density profile, modified to take into account the local density. The density, in turn, is the sum of a plasmaspheric profile and a high-latitude auroral profile.

$$\epsilon_{\perp} = (\text{low-density tabulated value}) + \frac{n\bar{m}}{B_0^2} \quad (2.1)$$

TODO: What's a clean way of showing the low-density ϵ_{\perp} that we read in?

TODO: Does Kelley list the electric constant or the Alfvén speed?

Where \bar{m} is the ambient mean molecular mass and B_0 is the zeroth-order magnetic field strength, $B_0 = 3.11 \times 10^4 \text{ nT} \left(\frac{R_E}{r}\right)^3 \sqrt{1 + 3 \cos^2 \theta}$. Note that $3.11 \times 10^4 \text{ nT}$ is the value of the Earth's magnetic field at the equator on Earth's surface.

TODO: Cite this number? Jesse just says it's a "representative" number. He uses 30 pT.

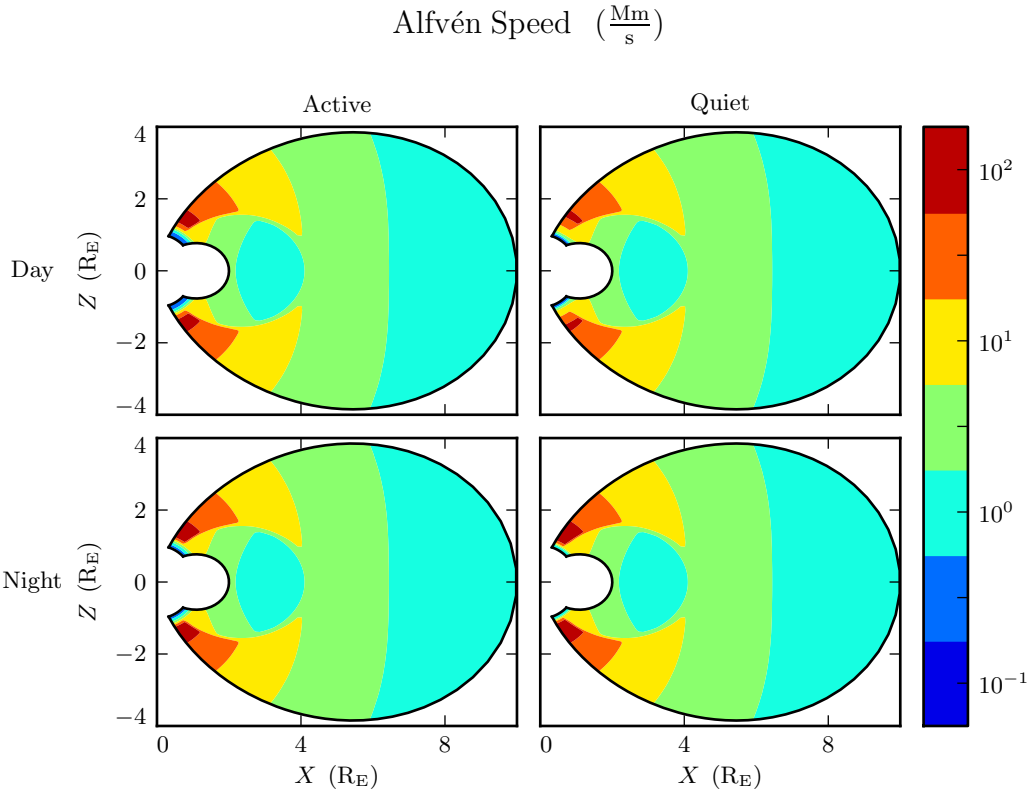


Figure 2.1: Alfvén speed profiles, adapted by Lysak[65] from Appendix B of Kelley's textbook[48].

TODO: Above the profile, Bob scales the value that's read in as r^5 or something. Is there a citation for that?

The Alfvén speed is then computed per $v_A^2 \equiv \frac{1}{\mu_0 \epsilon_{\perp}}$.

Alfvén Bounce Frequencies

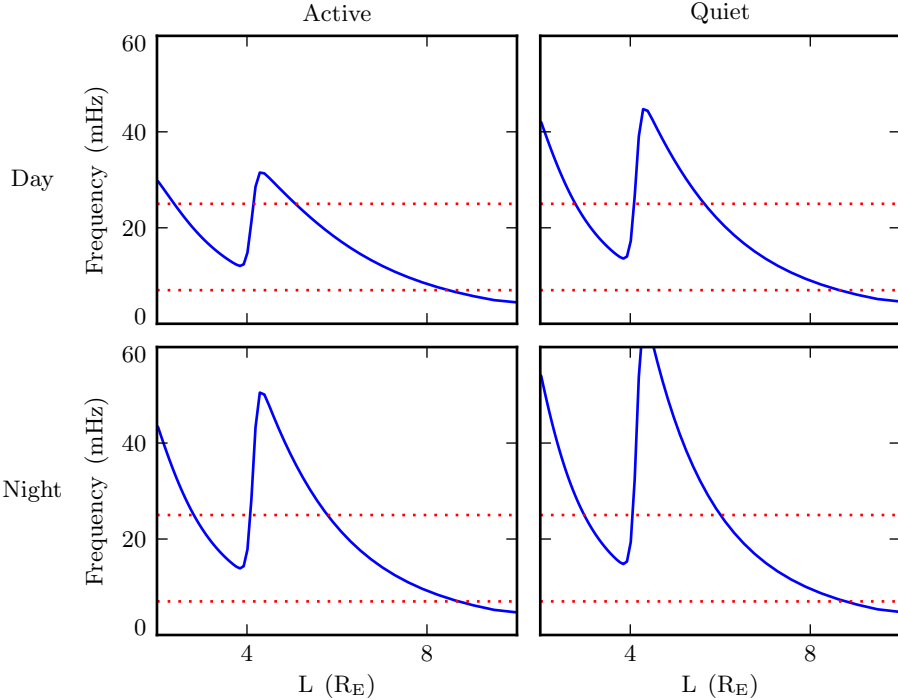


Figure 2.2: Alfvén bounce frequency profiles, computed by integrating the the Alfvén speed back and forth over a field line. $f_A = \left[\oint \frac{dz}{v_A} \right]^{-1}$. Dotted lines indicate the Pc4 frequency range, 7 mHz to 25 mHz. In each profile, the effect of the plasmapause is clearly visible, centered at $L = 4$. Field lines just inside and just outside the plasmapause appear susceptible to resonance in the Pc4 band.

TODO: Talk about how the size of the plasmasphere can be adjusted, and $4 R_E$ is just a typical value.

TODO: Explain how the Alfvén speed constrains the time step.

2.2 Waves in Cold Resistive Plasmas

TODO: Sketch out what a dispersion relation is, why it works, why it's interesting.

TODO: Explain that the inclusion of conductivity is novel.

TODO: This chapter works out the sorts of waves that might be expected in the numerical model. It starts with the same equations that are used by the model – Maxwell's equations and Ohm's Law. The resulting dispersion relation is too high-ordered for a direct solution, so several limits of interest are considered.

TODO: At this end of this chapter, there will be a discussion of what is specifically interesting about the findings. That doesn't really exist yet. Or... actually, should we discuss interesting things as we find them? Note that we find $\omega^2 = k^2 v_A^2$ several times.

Cold, linearized Ampère's Law and Faraday's Law. The vector \underline{B} is the perturbation to the zeroth-order magnetic field.

$$\frac{\partial}{\partial t} \underline{B} = -\nabla \times \underline{E} \quad \underline{\epsilon} \cdot \frac{\partial}{\partial t} \underline{E} = \frac{1}{\mu_0} \nabla \times \underline{B} - \underline{J} \quad (2.2)$$

Ohm's Law. Electron inertial effects are included in the parallel direction. See Chapter 4.

$$\frac{m_e}{ne^2} \frac{\partial}{\partial t} J_{\parallel} = \sigma_0 E_{\parallel} - J_{\parallel} \quad 0 = \underline{\sigma}_{\perp} \cdot \underline{E}_{\perp} - \underline{J}_{\perp} \quad (2.3)$$

Suppose that the fields and currents are resonating as $\exp(i\underline{k} \cdot \underline{x} - i\omega t)$. Evaluate the derivatives. Eliminate magnetic fields and currents.

$$\begin{aligned} 0 &= E_{\parallel} + \frac{c^2}{\omega^2} (\underline{k} \cdot \underline{E} - k^2 \underline{E})_{\parallel} + \frac{i\omega_P^2}{\omega(\nu - i\omega)} E_{\parallel} \\ 0 &= \underline{E}_{\perp} + \frac{v_A^2}{\omega^2} (\underline{k} \cdot \underline{E} - k^2 \underline{E})_{\perp} + \frac{i}{\epsilon_{\perp}\omega} \underline{\sigma}_{\perp} \cdot \underline{E}_{\perp} \end{aligned} \quad (2.4)$$

The above expression makes use of the vector identity $\underline{k} \times \underline{k} \times \underline{E} = \underline{k} \cdot \underline{E} - k^2 \underline{E}$. The

Alfvén speed, speed of light, plasma frequency, and parallel conductivity are defined in the usual way:

$$v_A^2 \equiv \frac{1}{\mu_0 \epsilon_{\perp}} \quad c^2 \equiv \frac{1}{\mu_0 \epsilon_0} \quad \omega_P^2 \equiv \frac{ne^2}{m_e \epsilon_0} \quad \sigma_0 \equiv \frac{ne^2}{m_e \nu} \quad (2.5)$$

Note that this definition of the Alfvén speed takes into account the displacement current correction which is important when v_A approaches c .

Equation (2.4) is then assembled into the usual dispersion tensor form:

$$0 = \left(\underline{\underline{\mathbb{I}}} + \frac{1}{\omega^2} \underline{\underline{V}}^2 \cdot \underline{k} \underline{k} - \frac{k^2}{\omega^2} \underline{\underline{V}}^2 + \frac{i}{\omega} \underline{\underline{\Omega}} \right) \cdot \underline{E} \quad (2.6)$$

Where $\underline{\underline{\mathbb{I}}}$ is the identity tensor and in x - y - z coordinates,

$$\underline{\underline{V}}^2 \equiv \begin{bmatrix} v_A^2 & 0 & 0 \\ 0 & v_A^2 & 0 \\ 0 & 0 & c^2 \end{bmatrix} \quad \text{and} \quad \underline{\underline{\Omega}} \equiv \begin{bmatrix} \frac{\sigma_P}{\epsilon_{\perp}} & \frac{-\sigma_H}{\epsilon_{\perp}} & 0 \\ \frac{\sigma_H}{\epsilon_{\perp}} & \frac{\sigma_P}{\epsilon_{\perp}} & 0 \\ 0 & 0 & \frac{\omega_P^2}{(\nu - i\omega)} \end{bmatrix} \quad (2.7)$$

In Equation (2.6), the expression in parentheses is the dispersion tensor, $\underline{\underline{D}}$. Nontrivial solutions exist only when $\det \underline{\underline{D}} = 0$. This gives rise to a seventh-order polynomial in ω , so rather than a direct solution it's necessary to consider limits of specific interest.

2.2.1 Parallel or Perpendicular Propagation

TODO: Parallel propagation is interesting because it's a naive representation of a field line resonance. Perpendicular propagation is interesting because the movement of energy across field lines is a topic of particular interest. In both cases, the cross terms in $\underline{k} \underline{k}$ vanish, decoupling the parallel and perpendicular polarizations.

TODO: Without loss of generality, the wave vector \underline{k} is presumed to lie in the x - z plane. The distinction between the azimuthal and crosswise directions is revisited in Section 2.2.3.

TODO: ACTUALLY: does this even matter? If we keep ϕ in there in addition to θ , does it cancel out? Seems like it should.

In the parallel and perpendicular propagation limits respectively, the parallel factors of the determinants of $\underline{\underline{D}}$ are:

$$\begin{aligned} 0 &= \omega^2 + i\nu\omega - \omega_P^2 \\ 0 &= \omega^3 + i\nu\omega^2 - (k^2c^2 + \omega_P^2)\omega - ik^2c^2\nu \end{aligned} \tag{2.8}$$

Both expressions in Equation (2.8) can be solved directly, though the solution to the (cubic) perpendicular propagation case is too long to be useful. After expanding with respect to a very large plasma frequency, the solutions can be written (for parallel and perpendicular propagation respectively):

$$\begin{aligned} \omega^2 &= \omega_P^2 - i\nu\omega_P + \dots \\ \omega^2 &= k^2c^2 + \omega_P^2 - i\nu\omega_P + \dots \end{aligned} \tag{2.9}$$

The first expression in Equation (2.9) – describing the parallel-polarized component of a parallel-propagating wave – doesn't describe a wave at all; there's no dependence on the wave vector k . Instead, it describes the plasma oscillation. The second expression is the O mode: a compressional wave, oscillating just above the plasma frequency, with a parallel electric field.

The perpendicular factors of the dispersion tensor's determinant, in the cases of parallel and perpendicular propagation respectively, are:

$$\begin{aligned} 0 &= \omega^4 + 2i\frac{\sigma_P}{\epsilon_\perp}\omega^3 - \left(2k^2v_A^2 + \frac{\sigma_P^2 + \sigma_H^2}{\epsilon_\perp^2}\right)\omega^2 - 2ik^2v_A^2\frac{\sigma_P}{\epsilon_\perp}\omega + k^4v_A^4 \\ 0 &= \omega^3 + 2i\frac{\sigma_P}{\epsilon_\perp}\omega^2 - \left(2k^2v_A^2 + \frac{\sigma_P^2 + \sigma_H^2}{\epsilon_\perp^2}\right)\omega - ik^2v_A^2\frac{\sigma_P}{\epsilon_\perp} \end{aligned} \tag{2.10}$$

First expression of Equation (2.10) can be solved directly. Noting that \pm and \oplus are

independent,

$$\omega = \left(\frac{\pm\sigma_H - i\sigma_P}{2\epsilon_{\perp}} \right) \oplus \sqrt{k^2 v_A^2 + \left(\frac{\pm\sigma_H - i\sigma_P}{2\epsilon_{\perp}} \right)^2} \quad (2.11)$$

This wave is propagating along the field line, so the Pedersen and Hall conductivities are small for the vast majority of its trajectory. Expanding, then, gives

$$\omega^2 = k^2 v_A^2 \oplus kv_A \frac{\sigma_H \pm i\sigma_P}{\epsilon_{\perp}} + \dots \quad (2.12)$$

The second expression of Equation (2.10) can also be solved directly, though its roots are impractically long. They are expanded with respect to small conductivities (as would be seen by a perpendicular-propagating wave at high altitude) and at large conductivity (representing the perpendicular-propagating wave within the ionosphere). Respectively,

$$\begin{aligned} \omega^2 &= k^2 v_A^2 \pm ikv_A \frac{\sigma_P}{\epsilon_{\perp}} + \dots \\ \omega^2 &= k^2 v_A^2 + \left(\frac{\sigma_H \pm i\sigma_P}{\epsilon_{\perp}} \right)^2 + \dots \end{aligned} \quad (2.13)$$

Equations (2.12) and (2.13) describe Alfvén waves: waves traveling at the Alfvén speed (shifted by the ionospheric conductivity) with electric fields perturbations perpendicular to the zeroth-order magnetic field.

2.2.2 High Altitude Limit

In the limit of large radial distance, where the density is very low, it's reasonable to neglect the Pedersen conductivity, the Hall conductivity, and the collision rate.

Without loss of generality, the wave vector \underline{k} can be presumed to lie in the x - z plane¹.

Whereas in Section 2.2.1 the parallel component of the determinant of the dispersion tensor could be factored out, the high altitude limit decouples the azimuthal component

¹The azimuthal-propagation case is discussed in Section 2.2.3

from those in the meridional plane. The azimuthal component gives, simply,

$$\omega^2 = k^2 v_A^2 \quad (2.14)$$

This solution is analogous to the results in Section 2.2.1: a wave propagating at the Alfvén speed, with electric field perturbation perpendicular to both the zeroth-order magnetic field and the wave vector.

The meridional components of the determinant of the high-altitude limit of the dispersion tensor give:

$$0 = \omega^4 - \left(k_{\parallel}^2 v_A^2 + k_{\perp}^2 c^2 + \omega_P^2 \right) \omega^2 + k_{\parallel}^2 v_A^2 \omega_P^2 \quad (2.15)$$

Where k_{\parallel} and k_{\perp} are the parallel and crosswise components of the wave vector. The a
Equation (2.15) is quadratic in ω^2 . Its solution is

$$\omega^2 = \frac{1}{2} \left(k_{\parallel}^2 v_A^2 + k_{\perp}^2 c^2 + \omega_P^2 \right) \pm \sqrt{\frac{1}{4} \left(k_{\parallel}^2 v_A^2 + k_{\perp}^2 c^2 + \omega_P^2 \right)^2 - k_{\parallel}^2 v_A^2 \omega_P^2} \quad (2.16)$$

Noting that ω_P is very large, the two roots simplify to

$$\begin{aligned} \omega^2 &= k_{\parallel}^2 v_A^2 + \dots \\ \omega^2 &= k_{\parallel}^2 v_A^2 + k_{\perp}^2 c^2 + \omega_P^2 + \dots \end{aligned} \quad (2.17)$$

TODO: The first part looks like an Alfvén wave. The second is faster than the plasma frequency, so we don't really care about it.

2.2.3 Implications for This Work

TODO: Have we got enough/appropriate math here to talk about how σ_H rotates fields at the ionosphere? Doubtful.

As m becomes large, it puts a lower bound on the modenumber, and thus on the

frequency. For an Alfvén wave, $\omega^2 = k^2 v_A^2$,

$$k \geq k_\phi = \frac{m}{2\pi r} \quad \text{so} \quad \omega \geq \frac{m}{2\pi r} v_A \quad (2.18)$$

Any wave with a frequency below this threshold will become evanescent.

TODO: This point is pretty important. It's revisited in Section 3.3.

Chapter 3

Numerical Model

TODO: Sketch out this chapter. What does 2.5 dimensions mean? Why is it an appropriate approach to this problem? Why is this model in particular a good fit? What previous similar work has been done? What's novel about this mode?

TODO: Also 2.5D: Waters 2013[103]. And Waters 2008[104].

Waters[103] cites Olson[73] with reference to modenumber.

The model works in two and a half dimensions. A meridional slice of the magnetosphere is resolved. Fields are presumed to vary azimuthally according to a fixed modenumber m . Derivatives in ϕ are replaced by im . Imaginary field values indicate a phase shift in the azimuthal direction.

TODO: From Bob's 2013 paper[65] (which was also 2.5D): "The shear Alfvén and compressional fast mode waves can be coupled not only by the Hall conductivity but also by inhomogeneities in the background plasma, which are unavoidable in a realistic magnetosphere [e.g., Lysak and Yoshikawa, 2006[66]; Waters et al., 2012[103]]. This coupling requires a finite wave vector component in the azimuthal direction, i.e., a finite m in the context of the present model. Because of the $\exp(im\phi)$ dependence assumed in this model, the coupling from the inhomogeneity enters as an imaginary part of the coupled wave fields with respect to the initial fields, whereas the Hall conductivity appears in phase with the initial fields. Thus, although a fully three-dimensional model

can give a more complete picture of wave propagation [e.g., Lysak, 2004[61]; Woodroffe and Lysak, 2012[105]], the present two-dimensional model serves to illustrate the nature of this coupling.”

The use of a fixed modenumber allows a dramatic decrease in computational cost. Waves with very high azimuthal modenumber are prohibitively expensive to simulate since they can only be resolved if grid resolution is very fine in the azimuthal direction.

TODO: Can we find a citation where someone explicitly talks about the computational cost of high- m simulations? Or is it just obvious Nyquist?

This prevents the simultaneous consideration of dayside and nightside phenomena, but is fine for azimuthally-localized waves. As was shown by [24], and recently confirmed in detail by [13], Pc4 pulsations are generally confined to just a few hours MLT on the dayside.

Driving with a compressional pulse from the outer boundary of a simulation is typical. This model also includes a novel driving mechanism: perturbations to the ring current.

The code is linear. All magnetic fields are a first-order perturbation over the zeroth-order dipole field. This is a not-great assumption out towards the magnetopause. In practice, however, most activity is within $L \sim 7 R_E$, where the dipole approximation is pretty good.

Models with height-resolved ionospheres are a very recent development. Lysak presented his in 2013[65].

Ground signatures are fairly recent as well.

TODO: Some ground signature work as far back as Greifinger and Greifinger in 1968[35], but there’s been steady advancement. Lysak and Song, in 2006, were the first to work out ground signatures without the assumption of a single-frequency wave.

TODO: The support software – the driver and the plotter – are significant too. Do they go in a section? In an appendix?

TODO: Past FLR simulations focused on a single mode, didn’t account well for the ionosphere, etc. Lee and Lysak 1989, 1990, 1991, Rankin et al 1993, 1995, 1999, Tikhonchuk

and Rankin 2000, 2002.

TODO: Past work that got ground signatures (without latitude-dependent zenith angle) Greifinger and Greifinger 1968, 1973, Hughes 1974, Sciffer and Waters 2002, Sciffer et al 2005. Better computation of ground signatures... Waters and Sciffer 2008, Sciffer and Waters 2011, Woodroffe and Lysak 2012.

Note that the model uses megameters, seconds, megacoulombs, and grams as the fundamental units of length, time, charge, and mass respectively. As a result, electric field is measured in mV/m, magnetic field is measured in nT, and Poynting flux is measured in mW/m². The electric constant is expressed in mF/m, not in units of ϵ_0 , not that it really matters.

3.1 Coordinate System

TODO: Past work which could be cited for geometry examples: Radoski 1967, Lee and Lysak 1989, 1991, Rankin et al 1993, 1994, Streltsov and Lotko 1995, 1999.

FLRs have traditionally been modeled by straightening the field lines into a rectangular configuration[19, 69], by unrolling the azimuthal coordinate into a cylindrical coordinate system[82], or through the use of dipole coordinates[81]¹:

$$x \equiv -\frac{\sin^2 \theta}{r} \quad y \equiv \phi \quad z \equiv \frac{\cos \theta}{r^2} \quad (3.1)$$

Where r , θ , and ϕ take on their usual spherical meanings of radial distance, colatitude, and azimuthal angle respectively.

The dipole coordinate x is constant over each equipotential shell², y is azimuthal angle, and z indexes each field line from south to north. The unit vectors \hat{x} , \hat{y} , and \hat{z} point in the crosswise³ (radially outward at the equator), azimuthal (eastward), and parallel

¹The dipole coordinates x , y and z are perhaps more commonly named μ , ϕ , and ν respectively; however, in the present work, μ and ν take other meanings.

²In fact, x is inversely proportional to the McIlwain parameter.

³In the context of in situ measurements taken near the equatorial plane, \hat{x} is referred to as the radial direction; however, the present work extends the dipole grid to low altitudes, where it can be more

(northward at the equator) directions respectively.

3.1.1 Differential Geometry

Notably, the dipole coordinates x , y , and z are normal to one another. While mathematically convenient, they do not readily accommodate a fixed-altitude boundary at the ionosphere, nor do they allow the dipole magnetic field to intersect the boundary at an oblique angle, as Earth's field does. As a solution, a nonorthogonal set of dipole coordinates was developed numerically by Proehl[79], then formalized analytically by Lysak[61] in terms of their contravariant components:

$$u^1 = -\frac{R_I}{r} \sin^2 \theta \quad u^2 = \phi \quad u^3 = \frac{R_I^2}{r^2} \frac{\cos \theta}{\cos \theta_0} \quad (3.2)$$

Above, R_I is the position of the ionosphere relative to Earth's center; it's typically taken to be $1 R_E + 100 \text{ km}$.

Like the dipole coordinates x , y , and z , Lysak's coordinates u^1 , u^2 , and u^3 correspond to L -shell, azimuthal angle, and position along a field line respectively. However, compared to z , u^3 has been renormalized using the invariant colatitude⁴ θ_0 . As a result, u^3 takes the value $+1$ at the northern ionospheric boundary and -1 at the southern ionospheric boundary for all u^1 and u^2 .

Because Lysak's coordinate system is not orthogonal⁵, it's necessary to consider covariant and contravariant basis vectors separately.

$$\hat{e}_i \equiv \frac{\partial}{\partial u^i} r \quad \hat{e}^i \equiv \frac{\partial}{\partial \underline{r}} u^i \quad (3.3)$$

Covariant basis vectors \hat{e}_i are normal to the curve defined by constant u^i , while contravariant basis vectors \hat{e}^i are tangent to the coordinate curve (or, equivalently, \hat{e}^i is

horizontal than vertical. The term "crosswise" is meant to indicate that \hat{x} is defined by the cross product of \hat{y} and \hat{z} .

⁴The invariant colatitude is the colatitude θ at which a field line intersects the ionosphere. It is related to the McIlwain parameter by $\cos \theta_0 \equiv \sqrt{1 - \frac{R_I}{L}}$.

⁵Curves of constant u^1 and curves of constant u^3 can intersect at non-right angles.

normal to the plane defined by constant u^j for all $j \neq i$). These vectors are reciprocal⁶ to one another, and can be combined to give components of the metric tensor $\underline{\underline{g}}$ [17].

$$\hat{e}^i \cdot \hat{e}_j = \delta_j^i \quad g_{ij} \equiv \hat{e}_i \cdot \hat{e}_j \quad g^{ij} \equiv \hat{e}^i \cdot \hat{e}^j \quad (3.4)$$

The metric tensor allows rotation between covariant and contravariant representations of vectors.

$$A_i = g_{ij} A^j \quad \text{and} \quad A^i = g^{ij} A_j \quad \text{where} \quad A_i \equiv \underline{A} \cdot \hat{e}_i \quad \text{and} \quad A^i \equiv \underline{A} \cdot \hat{e}^i \quad (3.5)$$

In addition, the determinant of the metric tensor⁷ is used to define cross products and curls⁸.

$$(\underline{A} \times \underline{B})^i = \frac{\varepsilon^{ijk}}{G} A_j B_k \quad \text{and} \quad (\nabla \times \underline{A})^i = \frac{\varepsilon^{ijk}}{G} \frac{\partial}{\partial u^j} A_k \quad \text{where} \quad G = \sqrt{g} \quad (3.6)$$

Explicit forms of the basis vectors and metric tensor can be found in the appendix of [61]. At present, it's sufficient to note the mapping between Lysak's basis vectors and the usual dipole unit vectors.

$$\hat{x} = \frac{1}{\sqrt{g^{11}}} \hat{e}^1 \quad \hat{y} = \frac{1}{\sqrt{g^{22}}} \hat{e}^2 \quad \hat{z} = \frac{1}{\sqrt{g^{33}}} \hat{e}^3 \quad (3.7)$$

The basis vectors can also be mapped to the spherical unit vectors, though Equation (3.8) is valid only at the ionospheric boundary.

$$\hat{\theta} = \frac{1}{\sqrt{g_{11}}} \hat{e}_1 \quad \hat{\phi} = \frac{1}{\sqrt{g_{22}}} \hat{e}_2 \quad \hat{r} = \frac{1}{\sqrt{g_{33}}} \hat{e}_3 \quad (3.8)$$

⁶The symbol δ_j^i is the Kronecker delta; the present work also makes use of the Levi-Civita symbol ε^{ijk} and Einstein's convention of implied summation over repeated indeces[20].

⁷Note $g \equiv \det \underline{\underline{g}}$.

⁸The quantity G is called the Jacobian determinant. It's sometimes denoted using the letter J , which the present work reserves for current.

3.1.2 Numerical Application

The coordinates converge at the equatorial ionosphere, so an inner boundary is necessary to maintain finite grid spacing. It's typically placed at $L = 2$. The outer boundary is at $L = 10$. The dipole approximation of Earth's magnetic field is tenuous at the outer boundary (particularly on the dayside); however, in practice, wave activity is localized inside $L \sim 7$. The grid is spaced uniformly in u^1 , which gives finer resolution close to Earth and coarser resolution at large distances.

Spacing in u^3 is set by placing grid points along the outermost field line. The points are closest together at the ionosphere, and grow towards the equator. The spacing increases in a geometric fashion, typically by 3%.

Most simulations take the grid to be 150 points in u^1 by 350 points in u^3 . The result is a resolution on the order of 10 km at the ionosphere, which increases to the order of 10^3 km at the midpoint of the outermost field line.

There are no grid points in u^2 , of course, because of the two and a half dimensional nature of the model. Fields are assumed to vary as $\exp(imu^2)$, so derivatives with respect to u^2 are equivalent to a factor of im . In effect, this means that the real component of each field is azimuthally in phase with the (purely real) driving, while imaginary values represent behavior that is azimuthally offset.

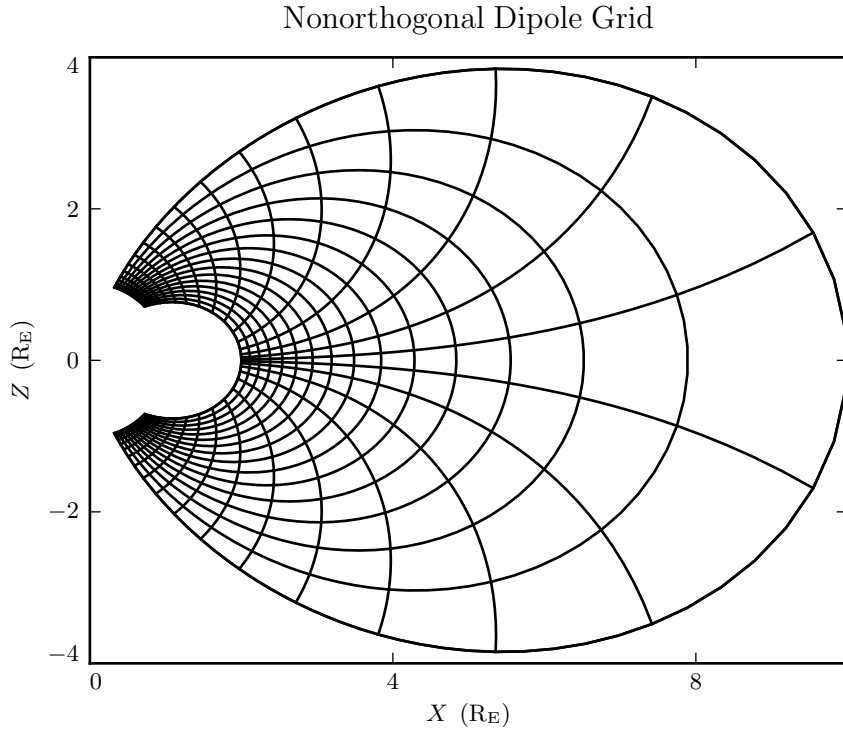


Figure 3.1: The model’s nonorthogonal dipole grid. Every fifth point is shown in each direction. The high concentration of grid points near Earth’s equator is a consequence of the coordinate system, which converges at the equatorial ionosphere.

The simulation’s time step is set based on the grid spacing. As is the convention, δt is set to match the smallest Alfvén zone crossing time, scaled down by a Courant factor (typically 0.1). It bears noting that the smallest crossing time need not correspond to the smallest zone; recall from Figure 2.1 that the Alfvén speed is very high in the Ionospheric Alfvén Resonator. A typical time step is on the order of 10^{-5} s.

TODO: Do we need a citation for how time steps are set based on crossing times?

3.2 Maxwell's Equations

TODO: Introduce Faraday's Law and Ampère's Law, respectively, after using Kirchhoff's formulation of Ohm's Law ($\underline{J} = \underline{\sigma} \cdot \underline{E}$) to eliminate explicit curl dependence... which will be revisited in Chapter 4.

$$\frac{\partial}{\partial t} \underline{B} = -\nabla \times \underline{E} \quad \underline{\epsilon} \cdot \frac{\partial}{\partial t} \underline{E} = \frac{1}{\mu_0} \nabla \times \underline{B} - \underline{\sigma} \cdot \underline{E} \quad (3.9)$$

TODO: Explain that we'll start in x - y - z coordinates – crosswise, azimuthal, and parallel – then map to the nonorthogonal basis at the very end. Otherwise it's necessary to carry around geometric factors.

3.2.1 Linearization and Optimization

TODO: Leapfrog grid (for which Waters[103] cites Taflove and Hagness, an electrodynamics textbook). Talk about the grid parity as well as the offset in time.

TODO: Precomputation of coefficients.

TODO: Curl shorthand, \underline{C} and \underline{F} . Recalling Equation (3.6),

$$C^i = \frac{\varepsilon^{ijk}}{G} \frac{\partial}{\partial u^j} E_k \quad F^i = \frac{\varepsilon^{ijk}}{G} \frac{\partial}{\partial u^j} B_k \quad (3.10)$$

TODO: OpenMP.

TODO: Keeping only covariant field components and contravariant curl components, since we only use contravariant coordinates.

3.2.2 Magnetic Fields

Taking the shorthand introduced in Equation (3.10), Faraday's Law can simply be written:

$$\frac{\partial}{\partial t} B^i = -C^i \quad (3.11)$$

Writing each component out explicitly, and using the metric tensor (per Equation (3.5)) to eliminate contravariant magnetic field components, Equation (3.11) becomes:

$$\begin{aligned} B_1 &\leftarrow B_1 - g_{11} \delta t C^1 - g_{13} \delta t C^3 \\ B_2 &\leftarrow B_2 - g_{22} \delta t C^2 \\ B_3 &\leftarrow B_3 - g_{31} \delta t C^1 - g_{33} \delta t C^3 \end{aligned} \quad (3.12)$$

Note that the \leftarrow operator is used in Equation (3.12) to indicate assignment, rather than equality. Terms on the left are new, while those on the right are old.

3.2.3 Electric Fields

Ampère's Law, as formulated in Equation (3.9), presents a nontrivial differential equation. Not only are the electric field values coupled to their own derivatives, but the crosswise and azimuthal components of the equation are coupled by the Hall terms in the conductivity tensor.

Fortunately, the permittivity tensor can be easily inverted, allowing a solution by integrating factor. Recalling the shorthand introduced in Equation (3.10),

$$\underline{\underline{\epsilon}} \cdot \frac{\partial}{\partial t} \underline{E} = \frac{1}{\mu_0} \underline{F} - \underline{\underline{\sigma}} \cdot \underline{E} \quad \text{becomes} \quad \left(\underline{\underline{\Omega}} + \underline{\underline{\epsilon}} \frac{\partial}{\partial t} \right) \cdot \underline{E} = \underline{V}^2 \cdot \underline{F} \quad (3.13)$$

Where $\underline{\underline{\mathbb{I}}}$ is the identity tensor and in x - y - z coordinates⁹,

$$\underline{\underline{V}^2} \equiv \frac{1}{\mu_0} \underline{\underline{\epsilon}}^{-1} = \begin{bmatrix} v_A^2 & 0 & 0 \\ 0 & v_A^2 & 0 \\ 0 & 0 & c^2 \end{bmatrix} \quad \text{and} \quad \underline{\underline{\Omega}} \equiv \underline{\underline{\epsilon}}^{-1} \cdot \underline{\underline{\sigma}} = \begin{bmatrix} \frac{\sigma_P}{\epsilon_\perp} & \frac{-\sigma_H}{\epsilon_\perp} & 0 \\ \frac{\sigma_H}{\epsilon_\perp} & \frac{\sigma_P}{\epsilon_\perp} & 0 \\ 0 & 0 & \frac{\sigma_0}{\epsilon_0} \end{bmatrix} \quad (3.14)$$

Multiplying through by $\exp(\underline{\underline{\Omega}} t)$ and applying the product rule, Equation (3.13) becomes¹⁰

$$\frac{\partial}{\partial t} \left(\exp(\underline{\underline{\Omega}} t) \cdot \underline{\underline{E}} \right) = \exp(\underline{\underline{\Omega}} t) \cdot \underline{\underline{V}^2} \cdot \underline{\underline{F}} \quad (3.15)$$

Equation (3.15) can then be integrated over a small time step δt and expressed in terms of the assignment operator introduced in Equation (3.11).

$$\underline{\underline{E}} \leftarrow \exp(-\underline{\underline{\Omega}} \delta t) \cdot \underline{\underline{E}} + \delta t \exp(-\underline{\underline{\Omega}} \frac{\delta t}{2}) \cdot \underline{\underline{V}^2} \cdot \underline{\underline{F}} \quad (3.16)$$

The tensor exponential can be evaluated by splitting $\underline{\underline{\Omega}}$ into the sum of its diagonal and Hall components¹¹. The Hall exponential condenses into sines and cosines, giving a rotation around the magnetic field line.

$$\underline{\underline{E}} \leftarrow \exp\left(-\underline{\underline{\Omega}}_D \delta t\right) \cdot \underline{\underline{R}}_z\left(\frac{-\sigma_H \delta t}{\epsilon_\perp}\right) \cdot \underline{\underline{E}} + \delta t \underline{\underline{V}^2} \cdot \exp\left(-\underline{\underline{\Omega}}_D \frac{\delta t}{2}\right) \cdot \underline{\underline{R}}_z\left(\frac{-\sigma_H \delta t}{2\epsilon_\perp}\right) \cdot \underline{\underline{F}} \quad (3.17)$$

Where

$$\underline{\underline{R}}_z(\theta) = \begin{bmatrix} \cos \theta & -\sin \theta & 0 \\ \sin \theta & \cos \theta & 0 \\ 0 & 0 & 1 \end{bmatrix} \quad \text{and} \quad \underline{\underline{\Omega}}_D \equiv \begin{bmatrix} \frac{\sigma_P}{\epsilon_\perp} & 0 & 0 \\ 0 & \frac{\sigma_P}{\epsilon_\perp} & 0 \\ 0 & 0 & \frac{\sigma_0}{\epsilon_0} \end{bmatrix} \quad (3.18)$$

⁹Note the parallel component of the present definition of $\underline{\underline{\Omega}}$ differs slightly from that used in Section 2.2.

¹⁰Tensor exponentiation is analogous to scalar exponentiation[37]: $\exp(\underline{\underline{T}}) \equiv \sum_n \frac{1}{n!} \underline{\underline{T}}^n$.

¹¹As long as the tensors $\underline{\underline{T}}$ and $\underline{\underline{T}'}$ commute – which is guaranteed if either is diagonal – $\exp(\underline{\underline{T}} + \underline{\underline{T}'}) = \exp(\underline{\underline{T}}) \exp(\underline{\underline{T}'})$.

The parallel component of term of Equation (3.17) is simply

$$E_{\parallel} \leftarrow E_{\parallel} \exp\left(\frac{-\sigma_0 \delta t}{\epsilon_0}\right) + c^2 \delta t F_{\parallel} \exp\left(\frac{-\sigma_0 \delta t}{2\epsilon_0}\right) \quad (3.19)$$

Or, in covariant terms,

$$E_3 \leftarrow E_3 \exp\left(\frac{-\sigma_0 \delta t}{\epsilon_0}\right) + c^2 \delta t (g_{31} F^1 + g_{33} F^3) \exp\left(\frac{-\sigma_0 \delta t}{2\epsilon_0}\right) \quad (3.20)$$

Using the conductivity profiles introduced in Section 1.1, the minimum value of $\frac{\sigma_0 \delta t}{\epsilon_0}$ is on the order of 10^3 , making $\exp\left(\frac{-\sigma_0 \delta t}{\epsilon_0}\right)$ far too small to be stored in a double precision variable¹². That is, this model takes E_3 (and, proportionally, E_{\parallel}) to be uniformly zero. This issue is revisited in Chapter 4.

The perpendicular components of Equation (3.17), mapped from the dipole basis to the covariant basis using Equation (3.7) and Equation (3.5), give the expressions:

$$\begin{aligned} E_1 + \frac{g^{13}}{g^{11}} E_3 &\leftarrow E_1 \cos\left(\frac{-\sigma_H \delta t}{\epsilon_{\perp}}\right) \exp\left(\frac{-\sigma_P \delta t}{\epsilon_{\perp}}\right) \\ &+ E_2 \sin\left(\frac{-\sigma_H \delta t}{\epsilon_{\perp}}\right) \exp\left(\frac{-\sigma_P \delta t}{\epsilon_{\perp}}\right) \sqrt{\frac{g^{22}}{g^{11}}} \\ &+ E_3 \cos\left(\frac{-\sigma_H \delta t}{\epsilon_{\perp}}\right) \exp\left(\frac{-\sigma_P \delta t}{\epsilon_{\perp}}\right) \frac{g^{13}}{g^{11}} \\ &+ F^1 \cos\left(\frac{-\sigma_H \delta t}{2\epsilon_{\perp}}\right) \exp\left(\frac{-\sigma_P \delta t}{2\epsilon_{\perp}}\right) \frac{v_A^2 \delta t}{g^{11}} \\ &+ F^2 \sin\left(\frac{-\sigma_H \delta t}{2\epsilon_{\perp}}\right) \exp\left(\frac{-\sigma_P \delta t}{2\epsilon_{\perp}}\right) \frac{v_A^2 \delta t}{\sqrt{g^{11} g^{22}}} \end{aligned} \quad (3.21)$$

¹²Not coincidentally, $\frac{\sigma_0}{\epsilon_0}$ can also be written $\frac{\omega_P^2}{\nu}$. At the ionosphere, the collision frequency ν is fast compared to the frequency of a ULF wave... but it's still slow compared to the plasma frequency.

and

$$\begin{aligned}
E_2 \leftarrow & -E_1 \sin\left(\frac{-\sigma_H \delta t}{\epsilon_{\perp}}\right) \exp\left(\frac{-\sigma_P \delta t}{\epsilon_{\perp}}\right) \sqrt{\frac{g^{11}}{g^{22}}} \\
& + E_2 \cos\left(\frac{-\sigma_H \delta t}{\epsilon_{\perp}}\right) \exp\left(\frac{-\sigma_P \delta t}{\epsilon_{\perp}}\right) \\
& - E_3 \sin\left(\frac{-\sigma_H \delta t}{\epsilon_{\perp}}\right) \exp\left(\frac{-\sigma_P \delta t}{\epsilon_{\perp}}\right) \frac{g^{13}}{\sqrt{g^{11} g^{22}}} \\
& - F^1 \sin\left(\frac{-\sigma_H \delta t}{2\epsilon_{\perp}}\right) \exp\left(\frac{-\sigma_P \delta t}{2\epsilon_{\perp}}\right) \frac{v_A^2 \delta t}{\sqrt{g^{11} g^{22}}} \\
& + F^2 \cos\left(\frac{-\sigma_H \delta t}{2\epsilon_{\perp}}\right) \exp\left(\frac{-\sigma_P \delta t}{2\epsilon_{\perp}}\right) \frac{v_A^2 \delta t}{g^{22}}
\end{aligned} \tag{3.22}$$

Note that the E_3 terms can be ignored at present. They are referenced in Chapter 4.

3.3 Driving

TODO: If no energy is added, the simulation is pretty boring. Everything just stays zero.

3.3.1 Outer Boundary Compression

TODO: It's traditional to drive from the outer boundary. Cite some examples. It's an analog for solar wind conditions. The analogy is clear at low modenumbers (large azimuthal wavelengths), but is plausible at high modenumber (small azimuthal wavelengths) as well, due to KH waves on the magnetopause, for example.

TODO: As discussed in Chapter 2 and again in Section 2.2.3, Alfvén waves become guided as the azimuthal modenumber becomes large. Energy delivered at the outer boundary, as a result, is unable to propagate across field lines to stimulate resonances in the inner magnetosphere.

TODO: Compressional driving is applied by setting the value of B_3 at the boundary. A typical scale is 10 nT.

TODO: Figure 3.2 demonstrates this issue. Note that the large values on the bottom row should be taken with a grain of salt; it's not clear that the simulation is reliable when waves are continuously forced against the boundary.

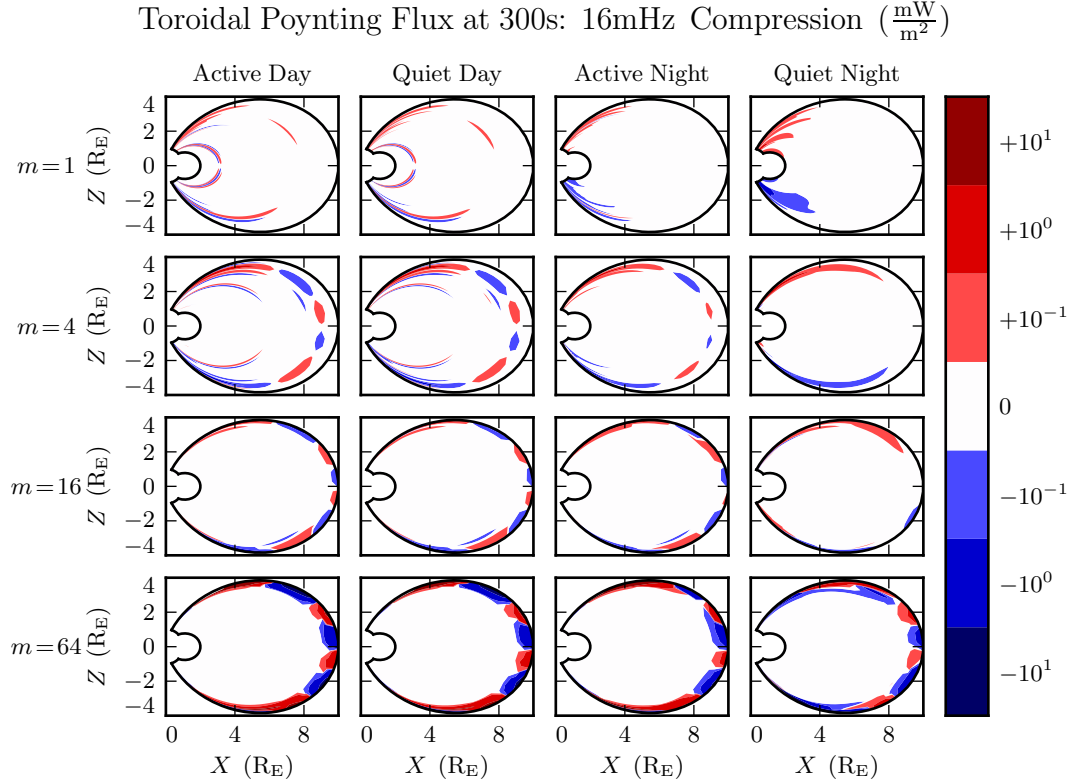


Figure 3.2: When the azimuthal modneumber is small, energy delivered through compression at the outer boundary propagates across field lines to stimulate resonances in the inner magnetosphere. However, as modenumber increases, Alfvén waves become increasingly guided. As a result, the inner magnetosphere is unaffected by perturbations at the outer boundary.

TODO: The present work, as a result, focuses mostly on simulations driven from within the magnetosphere.

3.3.2 Ring Current Modulation

TODO: Pc4 pulsations with high azimuthal modenumber have been shown to originate within the magnetosphere, such as through drift-resonant interactions with energetic radiation belt and ring current particles. Substorm injection can cause localized ring current behavior.

TODO: During and after geomagnetically active times, the ring current is a dynamic region. It's easy to imagine localized perturbations, though difficult to estimate their scale. The following is a kludgey estimate – better than no estimate at all!

TODO: The Sym-H storm index[72] measures magnetic perturbations on Earth's surface due to ring current activity. It's measured once per minute¹³, so Fourier amplitudes in the Pc4 range cannot be measured directly. However, they can be inferred by fitting the pink noise distribution. Figure 3.3 shows a Fourier series of the June 2013 storm and its recovery, along with its Fourier series coefficients. The red line shows a fit along the maximum of the Fourier coefficients.

TODO: Note that Sym-H is global and we're looking at localized perturbations! This is a conservative estimate, because it's averaged over the entire globe. Information on modenumbers comes from observations by Dai[13] and Takahashi[95], both of whom have seen fundamental-mode Pc4 pulsations with modenumbers of ~ 70 .

¹³Dst, the more commonly used storm index, is measured hourly.

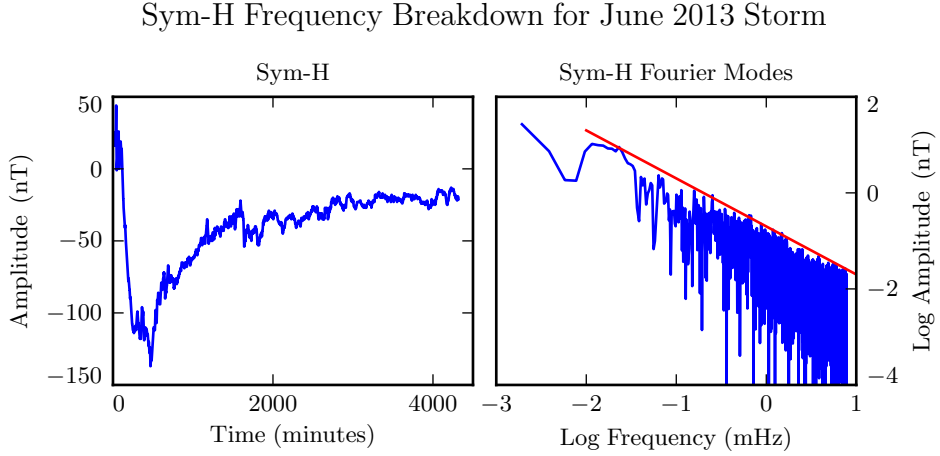


Figure 3.3: The Sym-H storm index[72] measures magnetic perturbations on Earth’s surface due to ring current activity. The amplitude of oscillations in the Pc4 range is estimated by fitting the Fourier amplitudes of the June 2013 storm.

TODO: $\tilde{B}(f) \sim 10^{-2} \text{ nT} \left(\frac{20 \text{ mHz}}{f} \right)$.

TODO: An oscillation with a period of about a minute could have an amplitude on the order of 10^{-2} nT .

TODO: Driving is typically delivered at $L = 5$, with a Gaussian spread of $0.5 R_E$ radially and 5° in latitude. Estimating the geometric factors from the size of the ring current, and from the fact that Sym-H is measured at Earth’s surface rather than at the center of the ring, this gives current density on the order of $10^{-4} \mu\text{A}/\text{m}^2$.

TODO: The driving current is applied by splitting the current in Ampère’s Law into an Ohmic term and a driving term:

$$\underline{\epsilon} \cdot \frac{\partial}{\partial t} \underline{E} = \frac{1}{\mu_0} \nabla \times \underline{B} - \underline{\sigma} \cdot \underline{E} - \underline{J}_{drive} \quad (3.23)$$

Equation (3.10) is then amended so that $\underline{F} \equiv \nabla \times \underline{B} - \underline{J}_{drive}$. As a result, no changes are necessary to Equations (3.20) to (3.22).

TODO: Effective peak driving electric field is...

3.4 Boundary Conditions

TODO: The grid can't go on forever. There have to be special cases at the edges.

3.4.1 Inner and Outer Boundaries

TODO: Recall that parity was already discussed in Section 3.2.1.

Dirichlet and Neumann boundary conditions are applied to the electric field components and magnetic field components respectively. That is, electric fields are forced to go to zero at the inner and outer boundaries, and magnetic fields are forced to have a zero derivative normal to the inner and outer boundaries.

These boundary conditions can in principle cause nonphysical reflections at the boundary¹⁴. However, in practice, wave activity is concentrated well within the simulation domain. Simulation results are robust under an exchange of Dirichlet and Neumann boundary conditions (though a self-inconsistent set of boundary conditions, such as applying Neumann boundary conditions to B_1 but Dirichlet boundary conditions to B_3 , quickly causes instability).

3.4.2 Coupling to the Atmosphere

Between the top of the neutral atmosphere and the bottom of the ionosphere, the model includes a thin, horizontal current sheet representing the ionosphere's E layer[61]. By integrating Ampère's Law over the layer, it can be shown[27] that the horizontal electric field values at the edge of the grid are determined by the jump in the horizontal magnetic fields:

$$\underline{\Sigma} \cdot \underline{E} = \lim_{\delta r \rightarrow 0} \left[\frac{1}{\mu_0} \hat{r} \times \underline{B} \right]_{R_I - \delta r}^{R_I + \delta r} \quad (3.24)$$

Like the height-resolved conductivities in Section 3.2.3, the tensor $\underline{\Sigma}$ is based on Kelley's[48] conductivity profiles. Parallel, Pedersen, and Hall conductivities are integrated from

¹⁴See, for example, the bottom row of Figure 3.2.

Earth's surface to the ionospheric boundary, then arranged (in θ - ϕ coordinates) as[61]:

$$\underline{\Sigma} \equiv \begin{bmatrix} \frac{\Sigma_0 \Sigma_P}{\Sigma_0 \cos^2 \alpha + \Sigma_P \sin^2 \alpha} & \frac{-\Sigma_0 \Sigma_H}{\Sigma_0 \cos^2 \alpha + \Sigma_P \sin^2 \alpha} \\ \frac{\Sigma_0 \Sigma_H}{\Sigma_0 \cos^2 \alpha + \Sigma_P \sin^2 \alpha} & \Sigma_P + \frac{\Sigma_H^2 \sin^2 \alpha}{\Sigma_0 \cos^2 \alpha + \Sigma_P \sin^2 \alpha} \end{bmatrix} \quad (3.25)$$

Where α is the angle between the magnetic field and the vertical direction, given by $\cos \alpha \equiv \frac{-2 \cos \theta}{\sqrt{1+3 \cos^2 \theta}}$.

An expression for the horizontal electric fields at the boundary can be obtained by inverting Equation (3.24). After mapping to covariant coordinates per Equation (3.8), and taking $\Sigma \equiv \det \underline{\Sigma}$,

$$\begin{aligned} E_1 &\leftarrow \frac{1}{\mu_0 \Sigma} \left[-\Sigma_{\theta\phi} B_1 - \sqrt{\frac{g_{11}}{g_{22}}} \Sigma_{\phi\phi} B_2 \Big|_{R_I-\delta r}^{R_I+\delta r} \right. \\ E_2 &\leftarrow \frac{1}{\mu_0 \Sigma} \left[\sqrt{\frac{g_{22}}{g_{11}}} \Sigma_{\theta\theta} B_1 + \Sigma_{\phi\theta} B_2 \Big|_{R_I-\delta r}^{R_I+\delta r} \right. \end{aligned} \quad (3.26)$$

The atmospheric magnetic field is computed as a linear combination of harmonics. The neutral atmosphere is considered to be a perfect insulator, giving $\nabla \times \underline{B} = 0$. Combined with $\nabla \cdot \underline{B} = 0$ (per Maxwell's equations), this allows the computation of a magnetic scalar potential Ψ such that $\underline{B} = \nabla \Psi$ and Ψ satisfies Laplace's equation, $\nabla^2 \Psi = 0$.

Laplace's equation can be solved analytically; however, a numerical solution is preferable to ensure orthonormality on a discrete and incomplete¹⁵ grid. After separating out the radial and azimuthal dependence in the usual way, the latitudinal component of Laplace's equation can be written in terms of $s \equiv -\sin^2 \theta$:

$$(4s^2 + 4s) \frac{d^2}{ds^2} Y_\ell + (4 + 6s) \frac{d}{ds} Y_\ell - \frac{m^2}{s} Y_\ell = \ell (\ell + 1) Y_\ell \quad (3.27)$$

Using centered differences to linearize the derivatives, Equation (3.27) becomes a system of coupled linear equations, one per field line. It can be solved numerically for

¹⁵As discussed in Section 3.1, the grid is constrained to finite L , which excludes the equator as well as the poles.

eigenvalues ℓ ($\ell + 1$) and eigenvectors¹⁶ Y_ℓ ¹⁷. In terms of the harmonics Y_ℓ , Ψ between the Earth's surface and the top of the atmosphere can be written

$$\Psi(r, \theta) = \sum_{\ell} \left(a_{\ell} r^{\ell} + b_{\ell} r^{-\ell-1} \right) Y_{\ell}(\theta) \quad (3.28)$$

As a boundary condition for Ψ , Earth is assumed to be a perfect conductor. This forces the magnetic field at Earth's surface to be horizontal; that is, $B_r = \frac{\partial}{\partial r} \Psi = 0$. Noting that solutions to Laplace's equation are orthonormal, each element of the sum in Equation (3.28) must be independently zero at R_E . This allows the coefficients a_{ℓ} and b_{ℓ} to be expressed in terms of one another.

$$b_{\ell} = \frac{\ell}{\ell + 1} R_E^{2\ell+1} a_{\ell} \quad (3.29)$$

The current sheet at the top of the atmosphere has been assumed to be horizontal, so the radial component of the magnetic field must be the same just above and just below it. Taking the radial derivative of Equation (3.28) at the top of the atmosphere, and eliminating b_{ℓ} with Equation (3.29), gives

$$B_r = \sum_{\ell} \ell a_{\ell} R_I^{\ell-1} \left(1 - \lambda_I^{2\ell+1} \right) Y_{\ell} \quad \text{where} \quad \lambda_I \equiv \frac{R_E}{R_I} \sim 0.975 \quad (3.30)$$

The summation can be collapsed by “integrating” over a harmonic¹⁸. Inverse harmonics can be obtained by inverting the eigenvector matrix. Then $Y_{\ell} \cdot Y_{\ell'}^{-1} = \delta_{\ell\ell'}$ by construction.

$$a_{\ell} = \frac{1}{\ell R_I^{\ell-1}} \frac{B_r \cdot Y_{\ell}^{-1}}{1 - \lambda_I^{2\ell+1}} \quad (3.31)$$

¹⁶The eigenvectors are not vectors in the same sense as \underline{B} and \underline{E} , of course; rather, they are scalar functions of θ defined on a discrete grid.

¹⁷Solving Laplace's equation analytically results in spherical harmonics indexed by both ℓ and m , the separation constants for θ and ϕ respectively. In two and a half dimensions, ϕ is not explicitly resolved, so m is set manually.

¹⁸Because the functions are defined on a discrete grid, their inner product is not an integral, but a sum:

$$B_r \cdot Y_{\ell}^{-1} \equiv \sum_i B_r[i] Y_{\ell}^{-1}[i].$$

Combining Equations (3.28), (3.29), and (3.31) allows the expression of Ψ at the top and bottom of the atmosphere as a linear combination of radial magnetic field components at the bottom of the ionosphere.

$$\begin{aligned}\Psi_E &= \sum_{\ell} Y_{\ell} \frac{R_I}{\ell} \frac{\frac{2\ell-1}{\ell-1} \lambda^{\ell}}{1 - \lambda_I^{2\ell+1}} B_r \cdot Y_{\ell}^{-1} \\ \Psi_I &= \sum_{\ell} Y_{\ell} \frac{R_I}{\ell} \frac{1 + \frac{\ell}{\ell-1} \lambda_I^{2\ell+1}}{1 - \lambda_I^{2\ell+1}} B_r \cdot Y_{\ell}^{-1}\end{aligned}\quad (3.32)$$

Horizontal magnetic fields are obtained by taking derivatives of Ψ .

$$B_1 = \frac{\partial}{\partial u^1} \Psi \quad B_2 = \frac{\partial}{\partial u^2} \Psi \quad (3.33)$$

Horizontal magnetic field values at the top of the atmosphere are used to impose boundary conditions on the electric fields at the bottom of the ionosphere, per Equation (3.26). Those at Earth's surface are valuable because they allow a direct comparison between model output and ground magnetometer data, after being mapped to physical coordinates per Equation (3.8).

Chapter 4

Electron Inertial Effects

TODO: Note that Bob's 2011 paper[64] had inertial effects.

TODO: Parallel electric fields and field-aligned currents are topics of particular interest.

The model described in Chapter 3 has the notable omission of parallel electric fields and parallel currents. That situation can be remedied by the addition of the electron inertial term in Ohm's Law.

4.1 Amending the Model

Old parallel electric field formulation. Recall $\underline{F} \equiv \nabla \times \underline{B}$.

$$\epsilon_0 \frac{\partial}{\partial t} E_{\parallel} = \frac{1}{\mu_0} F_{\parallel} - \sigma_0 E_{\parallel} \quad (4.1)$$

New parallel electric field formulation. The parallel current must now be tracked explicitly.

$$\epsilon_0 \frac{\partial}{\partial t} E_{\parallel} = \frac{1}{\mu_0} F_{\parallel} - J_{\parallel} \quad \frac{\partial}{\partial t} J_{\parallel} = \frac{ne^2}{m} E_{\parallel} - \nu J_{\parallel} \quad (4.2)$$

In the new formulation, J_{\parallel} (proportional to J_3) is solved with integrating factors and E_{\parallel} (E_3) can be advanced directly.

$$\begin{aligned} E_3 &\leftarrow E_3 + c^2 \delta t (g_{31} F^1 + g_{33} F^3) - \frac{\delta t}{\epsilon_0} J_3 \\ J_3 &\leftarrow J_3 \exp(-\nu \delta t) + \frac{ne^2}{m} \delta t E_3 \exp\left(-\nu \frac{\delta t}{2}\right) \end{aligned} \quad (4.3)$$

Recall that the electric and magnetic fields are staggered by half a time step. The current is defined with the magnetic fields, offset from the electric fields.

TODO: Note that simulations discussed in Chapters 5 and 6 do not include inertial effects. we just look at them here as a proof of concept. Resolving inertial length scales is too expensive, and not resolving them can easily lead to instability.

4.1.1 The Boris Approximation

Note that

$$\frac{\partial}{\partial t} E_{\parallel} \sim -\frac{1}{\epsilon_0} J_{\parallel} \quad \text{and} \quad \frac{\partial}{\partial t} J_{\parallel} \sim \frac{ne^2}{m_e} E_{\parallel} \quad \text{so} \quad \frac{\partial^2}{\partial t^2} E_{\parallel} \sim -\omega_P^2 E_{\parallel} \quad (4.4)$$

That is, the addition of the electron inertial term in Ohm's Law allows plasma oscillations.

As noted in Section 3.2.3, the plasma frequency is very large. Much larger than $\frac{1}{\delta t}$. But $\omega_P \delta t < 1$ is necessary for stability. In order to accommodate that condition, the time step in some runs would need to be dropped by three orders of magnitude; a simulation slated for one hour would suddenly take six weeks to complete.

TODO: This is a big deal! It's an additional constraint on the time step, in addition to the Alfvén crossing time.

The time step dictated by the Alfvén speed and grid spacing is typically on the order of 10 μ s, while the plasma frequency can be as small as 10 ns.

The plasma frequency (and the speed of light) can be decreased by taking an artificially

large value for ϵ_0 . Such approximations have been staples of numerical MHD models since Boris' work in 1970[5].

Lysak and Song[63] demonstrate the validity of such an approximation. To paraphrase their work, take Equation (4.2) and suppose that E_{\parallel} and J_{\parallel} are oscillating at a frequency ω . Then,

$$-i\omega\epsilon_0 E_{\parallel} = \frac{1}{\mu_0} F_{\parallel} - J_{\parallel} \quad -i\omega J_{\parallel} = \frac{ne^2}{m_e} E_{\parallel} - \nu J_{\parallel} \quad (4.5)$$

So

$$\left(1 - \frac{\omega^2 - i\nu\omega}{\omega_P^2}\right) E_{\parallel} = \frac{c^2}{\omega_P^2} (\nu - i\omega) F_{\parallel} \quad (4.6)$$

Here $\frac{c}{\omega_P}$ is the electron inertial length. While the speed of light and the plasma frequency each depend on ϵ_0 , their ratio does not. So long as $\left(1 - \frac{\omega^2 - i\nu\omega}{\omega_P^2}\right) \sim 1$, a change in ϵ_0 should not affect model behavior.

For the purposes of simulating ultra low frequency waves, Equation (4.6) allows perhaps-implausibly large Boris factors; even increasing ϵ_0 by a factor of 10^6 gives $\left|\frac{\omega^2 + i\omega\nu}{\omega_P^2}\right| \lesssim 0.01$. At that point, in some places, the speed of light is significantly slower than the Alfvén speed.

TODO: Ronnmark[83] calls this “anisotropic vacuum.”

TODO: This is common in other models... very high ionosphere, low speed of light, whatever. Cite LFM or something?

TODO: The plasma frequency is very fast compared to the waves we’re driving.

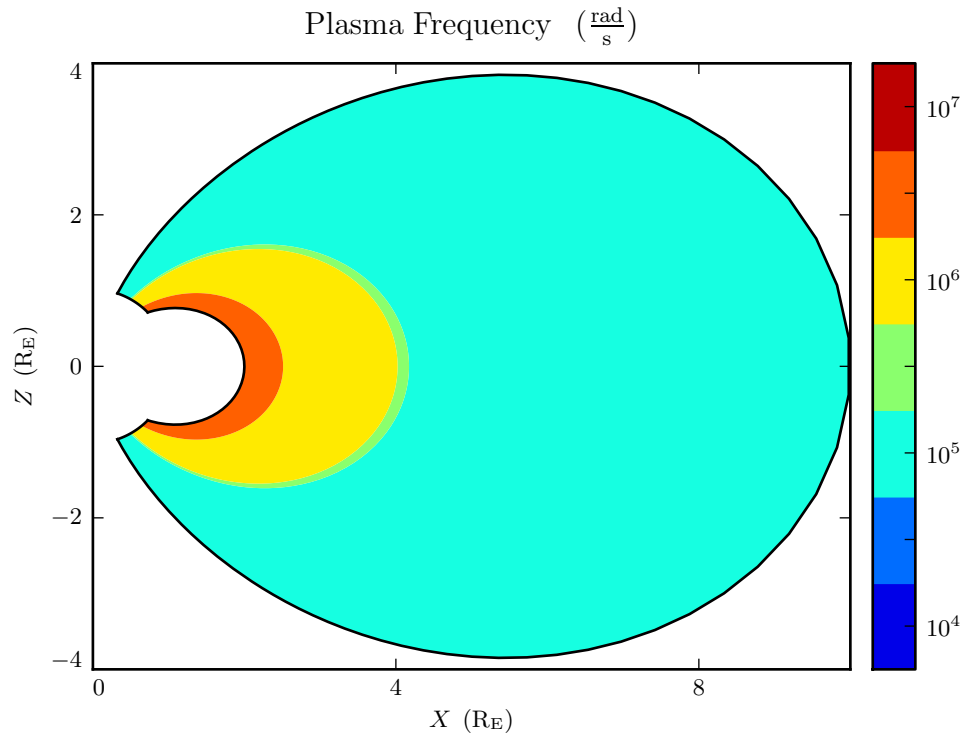


Figure 4.1: The plasma frequency reaches a peak value just under 10^7 rad/s near the equator. Outside the plasmasphere, its value is closer to 10^4 rad/s.

4.2 Quantifying the Results

TODO: How much does electron inertia matter?

TODO: Note, again, that only the figures in the present chapter include electron inertia. Those in Chapters 5 and 6 do not, for the sake of stability and computational cost.

4.2.1 Parallel Electric Fields

TODO: Even side-by-side, the magnetic fields in an otherwise-identical run are not visibly affected by the addition of electron inertial effects.

TODO: The parallel electric fields do a bit better... after all, any change is a big change compared to zero. But they're still very small.

With a bit of algebra, the meridional components of the dispersion tensor from Section 2.2.2 provide a comparison of the parallel and perpendicular electric field magnitudes.

$$\frac{E_{\parallel}}{E_{\perp}} = \frac{-k_{\parallel}k_{\perp}c^2}{\omega^2 - k_{\perp}^2c^2 - \omega_P^2} \sim \frac{k^2c^2}{\omega_P^2} \quad (4.7)$$

The electron inertial length $\frac{c}{\omega_P}$ is on the order of 1 km, smaller than the wavelength of a field line resonance by three or four orders of magnitude. That is, at high altitude, the parallel electric field is expected to be smaller than the perpendicular electric field by a factor of 10^7 – perhaps more, depending on how closely the wave vector is aligned to the magnetic field. That seems fine – note that Figure 4.2 shows that $\max E_{\parallel}$ is 4 to 5 orders larger than $\max E_{\perp}$... plus high altitude is the parallel field's minimum and the perpendicular field's maximum.

Electric Field Snapshots ($\frac{\text{mV}}{\text{m}}$): Quiet Day, 10mHz Current, $m = 16$

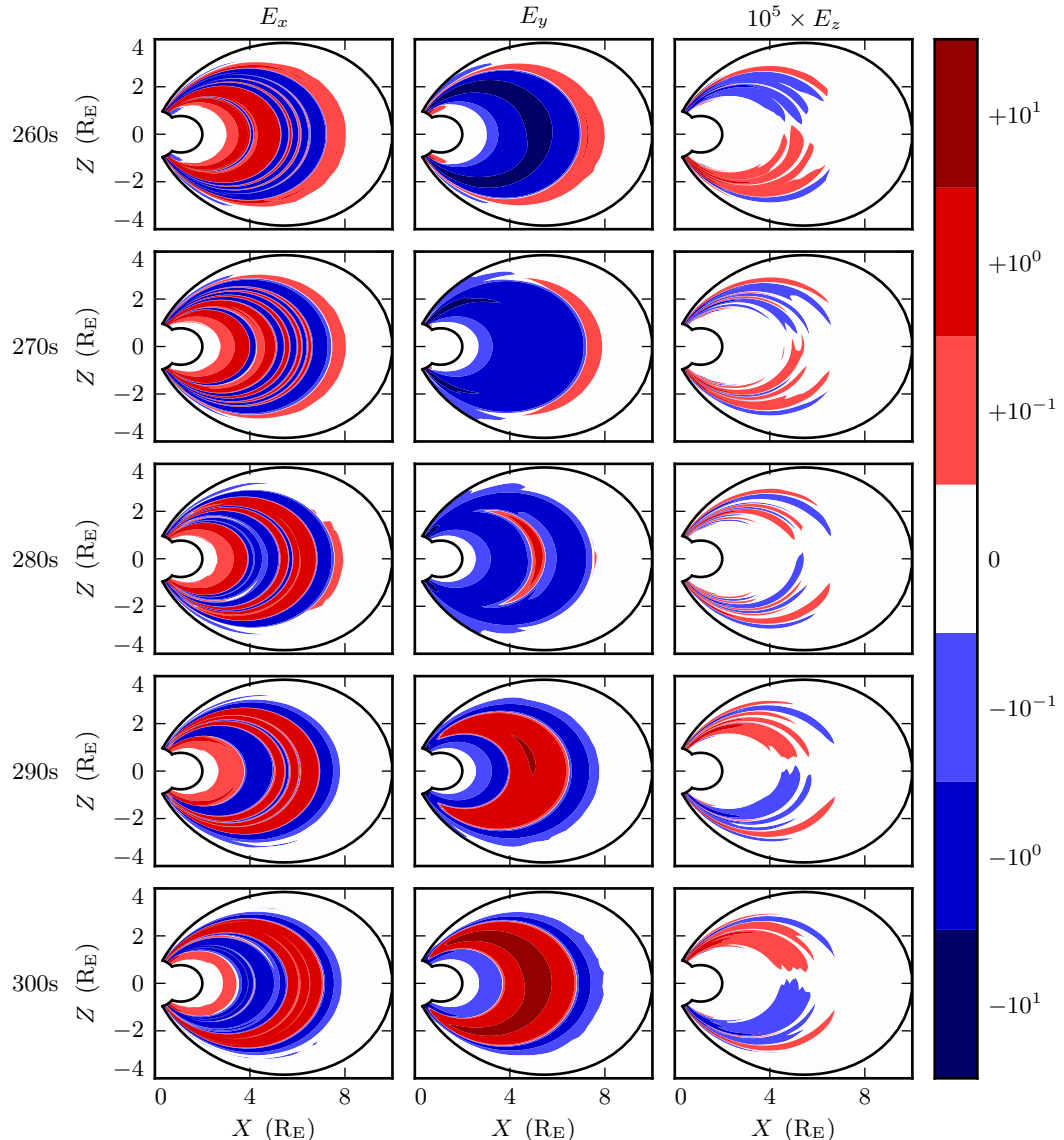


Figure 4.2: Parallel electric fields are smaller than perpendicular electric fields by at least four orders of magnitude.

4.2.2 Field-Aligned Current

TODO: The field-aligned current activity lines up with the Poynting flux. Poloidal Poynting flux is calculated from real E_y and B_x . Toroidal Poynting flux is imaginary E_x and B_y . The real component of the field-aligned current matches up with the poloidal, and the imaginary component lines up with the toroidal.

TODO: Over the bulk of the simulation, each field is overwhelmingly either real or imaginary. However, that gets muddled at the ionosphere by the Hall conductivity (rather than being purely a function of azimuthal derivatives).

Field-Aligned Current and Poynting Flux at R_I : Active Day, 16mHz Current

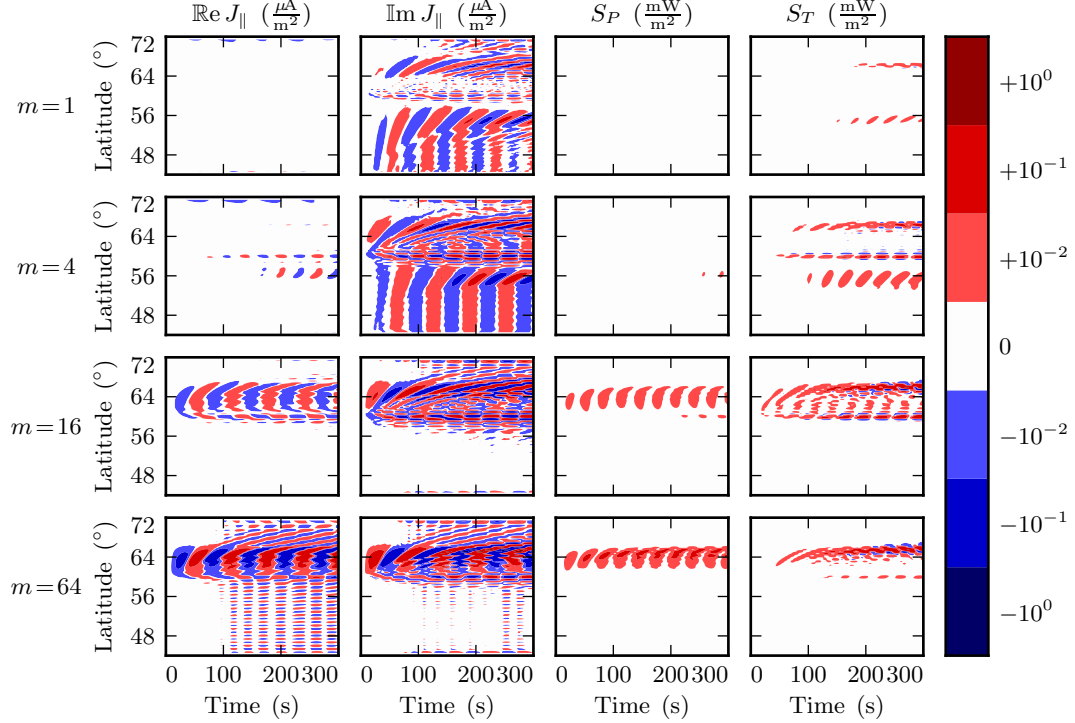


Figure 4.3: Perhaps unsurprisingly, field-aligned current structures at the ionospheric boundary line up with Poynting flux structures. The imaginary component of the current lines up with the toroidal Poynting flux (which is the product of imaginary E_x and imaginary B_y), while the real current lines up with the poloidal Poynting flux (E_y and B_x are real).

TODO: Notably, while the net Poynting flux is downward almost everywhere, field-aligned currents alternate between upward and downward flow. Perhaps this has to do with Poynting flux being a quadratic quantity while current is linear?

The “wiggles” visible in the lower-left corner of Figure 4.3 suggests overcorrection due to an improperly-coarse grid. See Section 4.2.3.

TODO: Field-aligned currents can be of significant size, but they’re not particularly

good at depositing energy in the ionosphere. As would be expected from energy conservation, $\nabla \cdot \underline{S}$ closely resembles $\underline{J} \cdot \underline{E}$, but only a vanishingly small portion of that is due to $J_z E_z$.

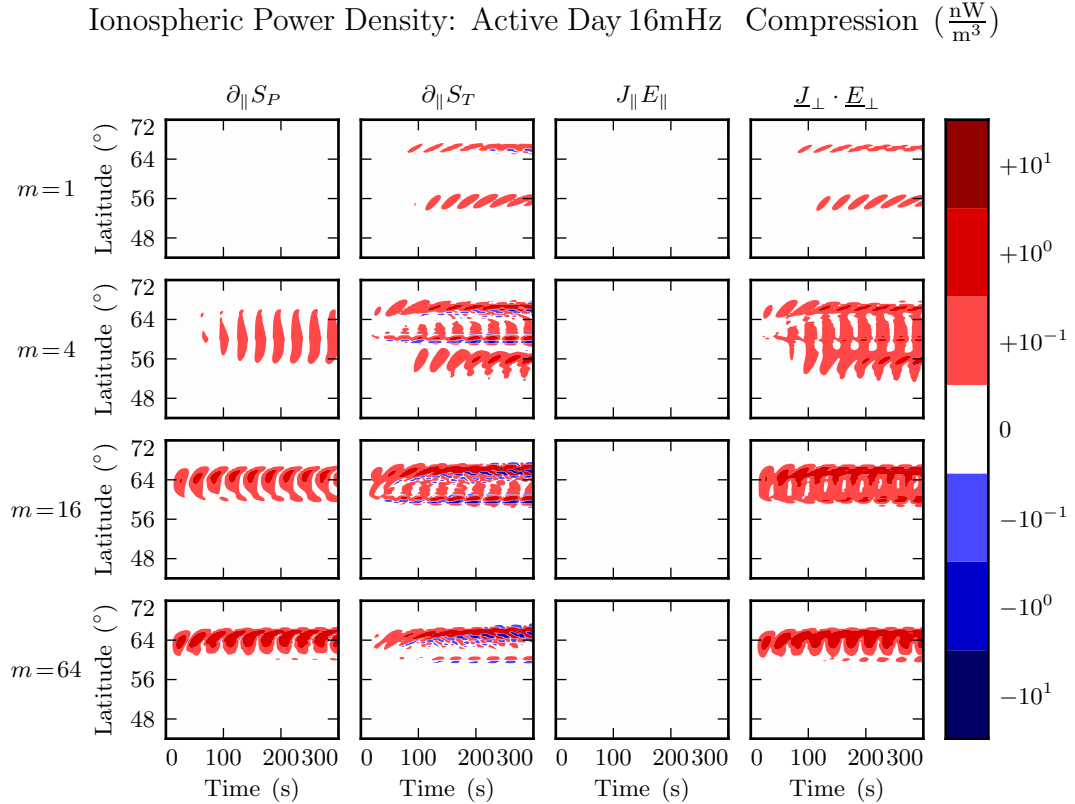


Figure 4.4: While field-aligned currents can be of significant size, they are not particularly good at depositing energy in the ionosphere. Energy deposited by the Poynting flux matches closely with Joule dissipation from the perpendicular currents – energy conservation! – while $J_{\parallel} E_{\parallel}$ is smaller by several orders of magnitude.

4.2.3 Inertial Length Scales

TODO: Are we really computing the electric fields faithfully? As touched on in Section 4.2.1, the perpendicular wavelength is important for determining the strength of

the parallel electric field. This is because everything depends on derivatives, not magnitudes.

TODO: A typical run has maximum perpendicular electric field on the order of 10 mV/m . Maybe a bit more. Field structures vary on the order of as little as $\sim 1^\circ$. That could give up to $\nabla \times \underline{E} \sim 10^2 \text{ nT/s}$. In comparison parallel electric fields max out around 10^{-3} mV/m . If that varies as a scale of the inertial length – as we expect, recalling Section 4.1.1 – that’s order of 1 km, it could give $\nabla \times \underline{E} \sim 1 \text{ nT/s}$. Plausibly large enough to have a visible effect. Note that the electron inertial length only needs to be resolved in the perpendicular direction, since that’s where we’re taking curls of the parallel electric field... which is the only quantity expected to change significantly (to lowest order) as a result of electron inertial effects.

TODO: This poses a significant computational cost. Within the plasmasphere, the inertial length is on the order of 0.1 km. That’s two-plus orders of magnitude smaller than the present grid. Moving the inner boundary from $L = 2$ to $L = 5$ makes up half of that.

TODO: We do a few runs which sorta resolve the electron inertial length. It’s about 2 km, and we get resolution down to 0.7 km. This is a factor of ten increase in resolution, and an additional factor of ten decrease in the time step (due to the drop in Alfvén crossing time). It’s not enough. Figure 4.5 is clearly not well-resolved. Those wiggles are probably about to cause a crash.

Parallel Electric Field ($\frac{\text{mV}}{\text{m}}$): Quiet Day, 100s of 16mHz Current, $m = 16$

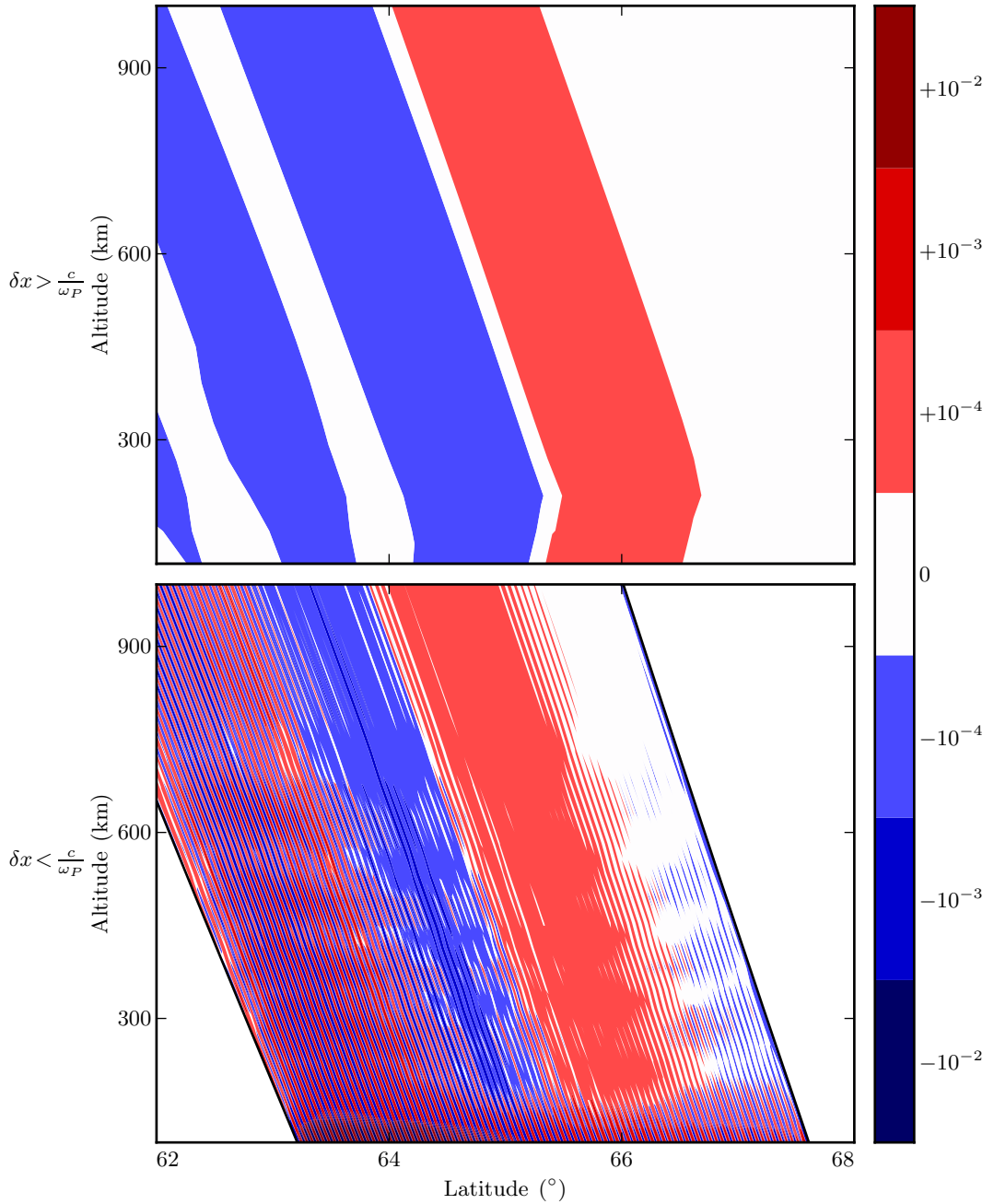


Figure 4.5: The parallel electric field develops significant structure when the perpendicular grid resolution is smaller than the electron inertial length. Unfortunately, such runs are prohibitively expensive. The lower panel – which still fails to resolve wave structure properly – represents a 100-fold increase in computational time.
52

TODO: The moral of the present section is that proper handling of electron inertial effects will probably show additional structure at small scales... but that simulating those structures is computationally expensive in terms of computational expense, even in 2.5D.

Chapter 5

Large Modenumber Effects

TODO: This chapter is the real moneymaker. The overarching motivation for this work is that $Pc4$ pulsations vary in interesting ways with respect to azimuthal modenumber, and that prior models have been unable to give a good picture of that behavior.

5.1 Finite Poloidal Lifetimes

Radoski[82] looked at Alfvén waves, using a cylindrical coordinate system to imitate an “unwrapped” dipole. He argued that poloidal waves should asymptotically rotate to the toroidal mode.

Mann[69] performed some wave-in-a-box simulations and found the rotation time to be linear in modenumber: $\tau = \frac{d\lambda}{d\omega'_A}$, where $\lambda = \frac{m}{2\pi r}$ and ω'_A is the spatial derivative of the Alfvén bounce frequency. Soon afterwards[70], he supported his simulations analytically.

TODO: Crunch out $\frac{d\lambda}{d\omega'_A}$. Preliminary indications are that it doesn’t translate well to a realistic grid, but let’s double check.

Ding[18] ran simulations more-or-less concurrent with Mann’s. Ding saw a rotation from poloidal to toroidal... then back again. It seems that the reversal was a spatial resolution issue.

The aforementioned models made significant simplifying assumptions in terms of geometry and boundary conditions.

Mann used straight field lines, a uniform Alfvén speed gradient, and perfectly conducting boundaries.

Ding's simulation is nominally carried out in a dipole geometry, but the ionospheric boundary is at $2.5 R_E$. Boundaries are also perfectly conducting.

That is, the results below offer a significantly higher level of realism than any past simulation (in part, of course, because computers are a lot better than they were 20 years ago).

A dedicated 3D treatment of this problem is unlikely at present. Large azimuthal modenumbers are expensive to compute. That's the whole point!

The energy is obtained by integrating (using the Jacobian to handle the grid properly) $U = \int dU = \int u dV$. Values are the log (base 10) of that, in the slightly odd units of gigajoules per radian. A factor of 2π wouldn't change anything, of course, but it seems inappropriate to integrate all the way around the sphere when $Pc4s$ are longitudinally localized (a fact which was an important part of justifying a 2.5D approach).

5.1.1 High Conductivity

In Figure 5.1, the rotation of energy from the poloidal mode to the toroidal mode is clear. Driving is strictly poloidal, yet the toroidal mode accumulates energy over time, and doesn't appear to give it back. The rotation happens faster for low- m simulations, qualitatively consistent with Mann's result; the time at which poloidal and toroidal energies are equal seems to even be linear in m , in line with his result.

At least, this is the case on the dayside, where the ionosphere is highly conductive.

Poloidal (Blue) and Toroidal (Red) Energy: Active Day

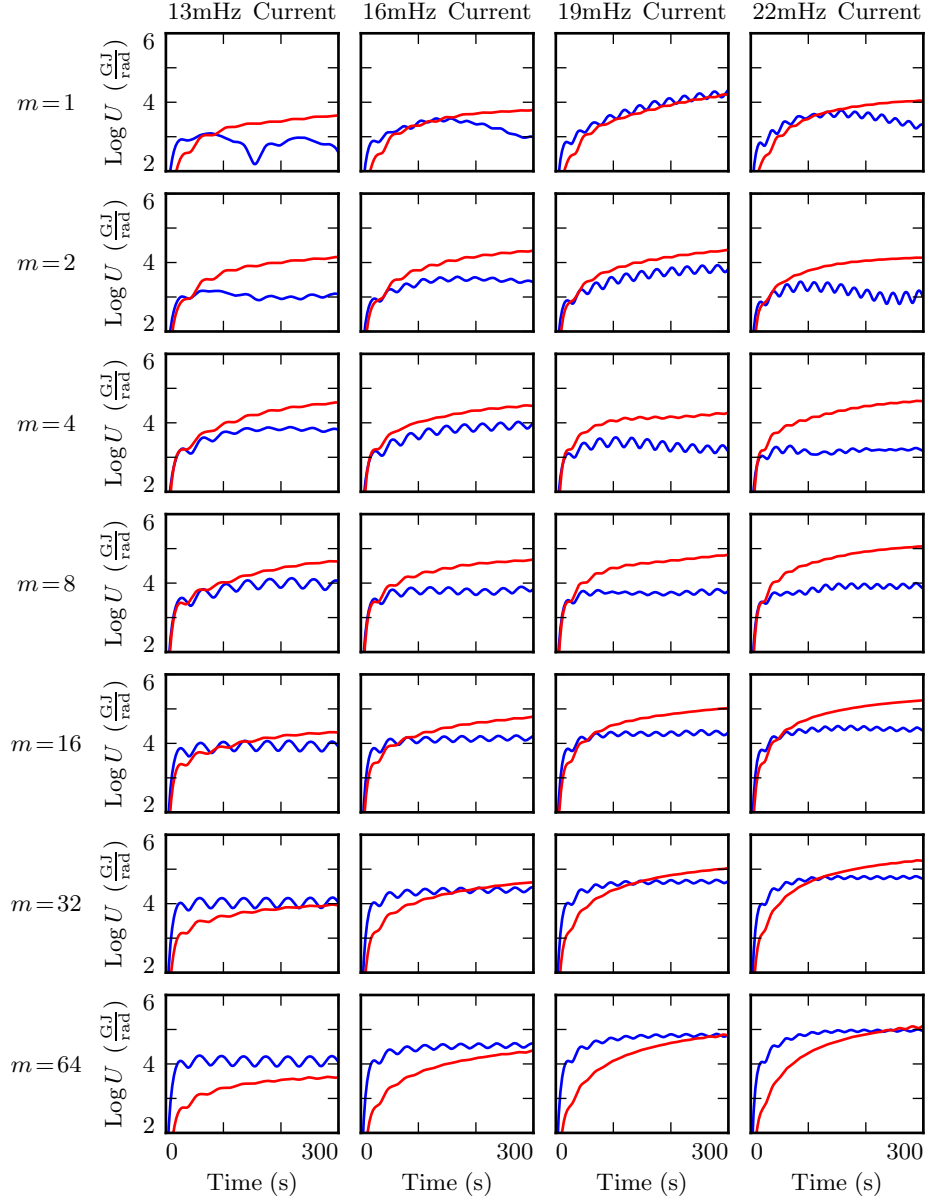


Figure 5.1: Driving is applied to the poloidal electric field. Over time, the energy rotates from the poloidal mode to the toroidal. The rotation rate is affected by the azimuthal modenumber.

5.1.2 Low Conductivity

The picture on the nightside (where the ionospheric conductivity is low) is significantly different from the dayside (where it's high).

Dissipation seems to outstrip rotation. Energy does not accumulate over numerous driving periods, as would be expected in resonance; it follows the driving up and down, as a damped-driven oscillator.

There is evidence that the rotation is still trying to happen. At low m , energy is distributed between the poloidal and toroidal mode before dissipating; at high m , the energy dissipates straight out of the poloidal mode, never having had a chance to rotate.

Poloidal (Blue) and Toroidal (Red) Energy: Quiet Night

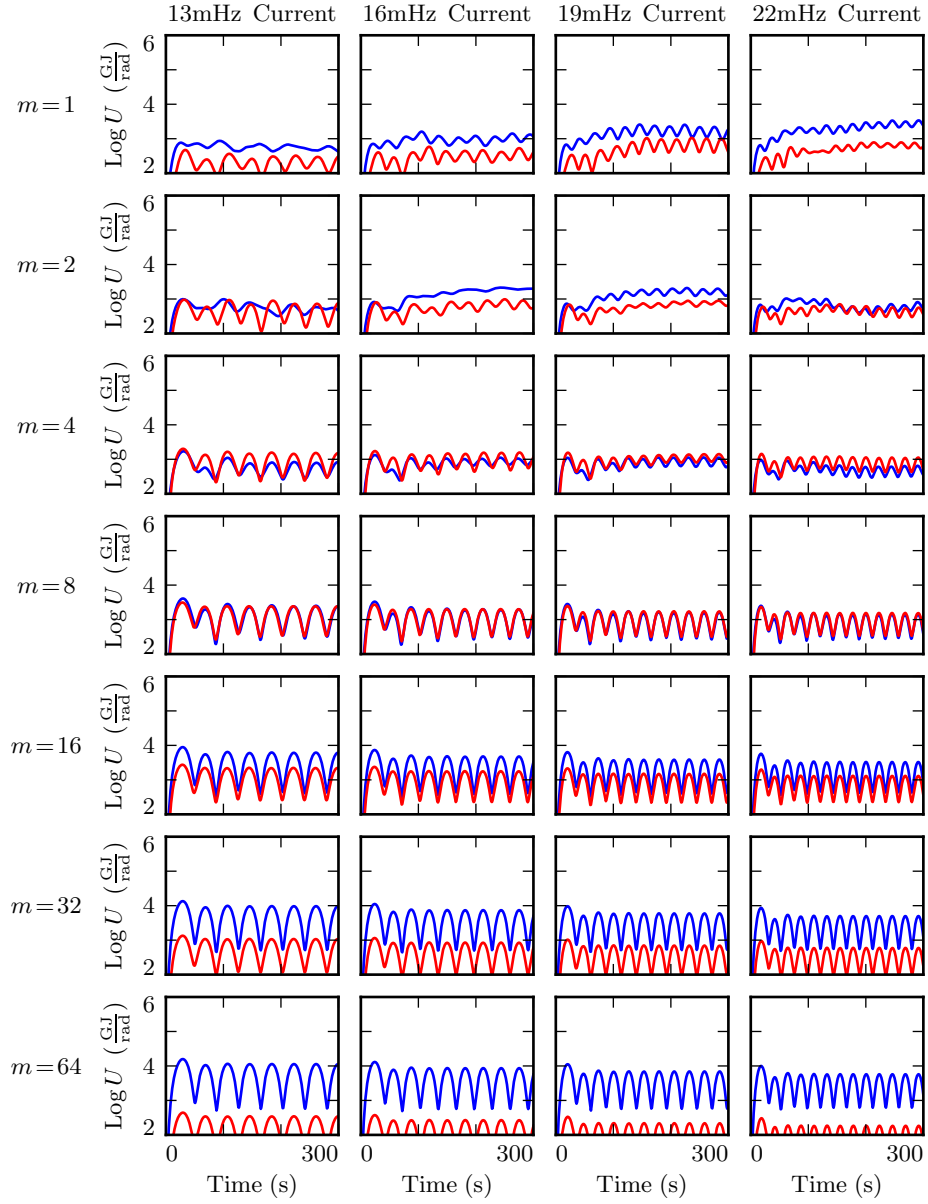


Figure 5.2: Driving is applied to the poloidal electric field. There is some rotation of energy to the toroidal mode (and less at high azimuthal modenumber), but the low ionospheric conductivity prevents energy from accumulating over time.

5.2 Spatial Distribution of Energy

Looking a bit deeper, it's possible to comment on the structure of the poloidal and toroidal modes, not just their magnitudes. The following commentary addresses the dayside; on the nightside, there's never much by the way of resonance.

In Figures 5.3 and 5.4, electromagnetic energy is binned by field line, averaged over volume (again, with respect to the Jacobian), and plotted as contours. All plots share a color scale.

The poloidal mode and the toroidal mode exhibit qualitatively different behavior, related to the fact that energy rotates from poloidal to toroidal, and not back.

At low m , energy rotates out of the poloidal mode so quickly that no resonance can form.

At high m , the Alfvén wave is guided. If the driving frequency lines up with the resonant frequency where it's delivered, the poloidal mode resonates strongly. Otherwise, again, no energy accumulates.

In no case does the poloidal mode demonstrate the ability to move energy across magnetic field lines.

On the other hand, the toroidal mode does resonate, even if the driving isn't resonant (though in that case the response is of course stronger). The toroidal mode transports energy across field lines until it encounters resonance, then accumulates energy there. Often, resonances are seen in multiple locations due to the non-monotonic Alfvén bounce frequency (recall Figure 2.2) as a function of L .

5.2.1 Resonant Driving

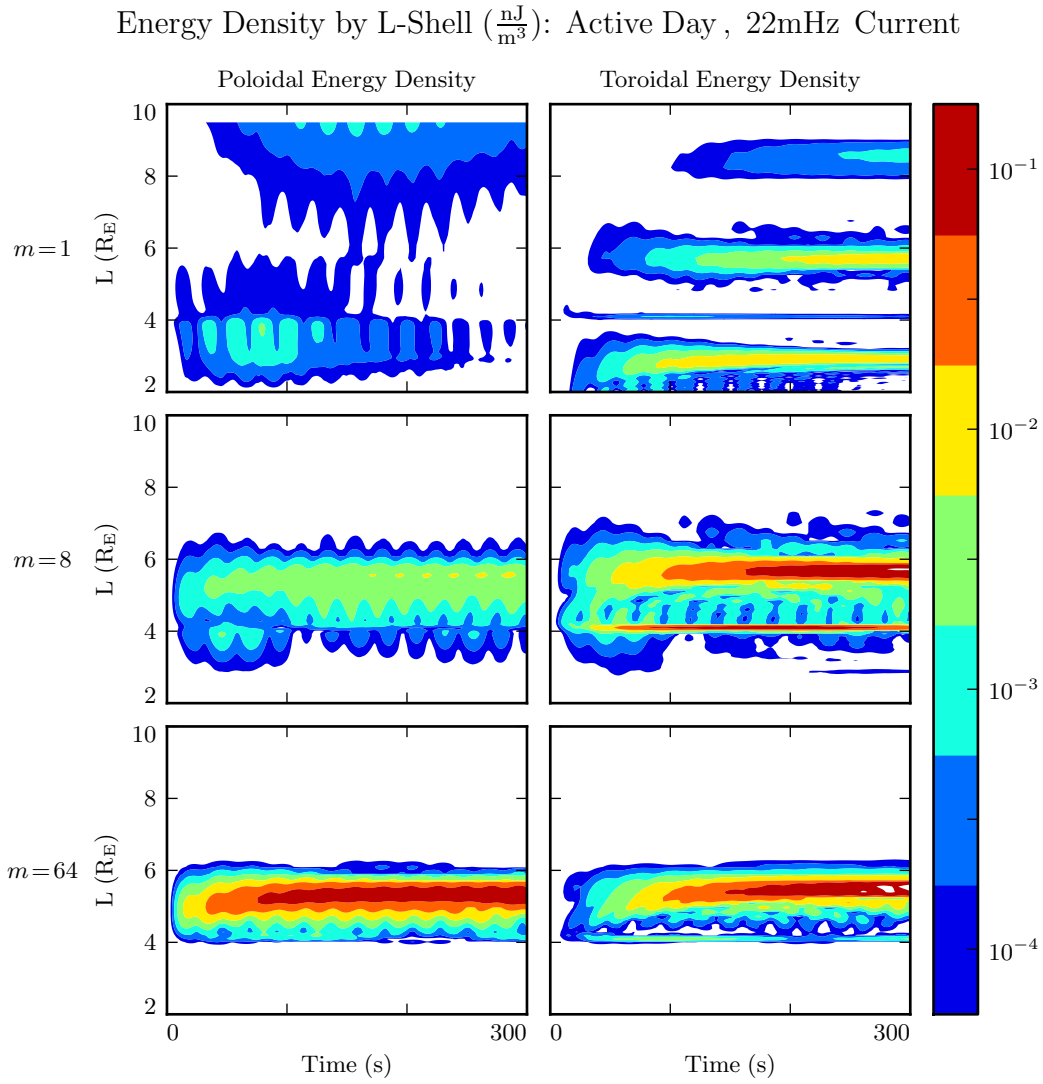


Figure 5.3: If m is small, energy rotates to the toroidal mode too fast to form a poloidal resonance. If m is large, the Alfvén wave is guided, so it resonates only if the driving frequency lines up with the resonant frequency where it's applied. The result is just one big – or perhaps even giant – pulsation. If the driving lines up with a nearby field line, the toroidal mode goes crazy! Resonance inside the plasmasphere. Resonance at the plasmapause. Resonance at the driving location. And (weak) attempt at a higher harmonic further out.

5.2.2 Nonresonant Driving

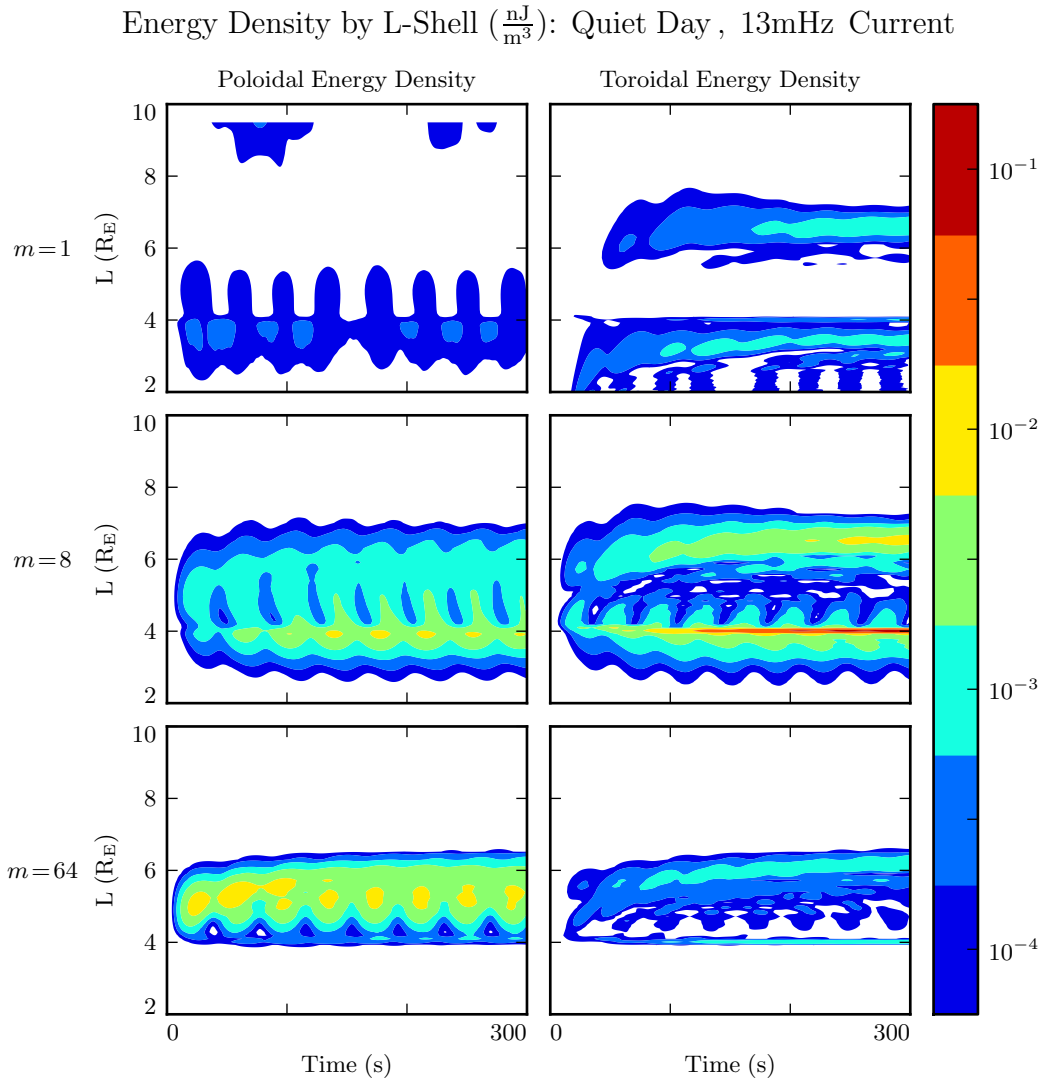


Figure 5.4: When the driving frequency doesn't line up with the location where it's delivered, there's basically no response. There is no movement of energy to a resonant field line, so no energy can accumulate over the course of multiple rounds of driving. Even when not driven resonantly, the toroidal mode still makes the best of its situation. It steals what energy it can from the poloidal mode, carries it to the resonant L -shell, and gets to work. (In contrast, recall from Figure 5.3, in this situation the poloidal mode just does not accumulate energy.) 63

5.3 Significance for Giant Pulsations

Giant pulsations are (probably[94]) fundamental mode poloidal $Pc4$ pulsations with frequencies around 10 mHz and azimuthal modenumber around 20. They are large, and can sometimes be observed on the ground.

While this model makes no particular distinction between a giant pulsation and any other $Pc4$, the above results do line up with giant pulsation observations.

Giant pulsations aren't seen at small m . As shown in Section 5.1, low- m poloidal modes rotate to the toroidal mode too quickly to resonate effectively, even in the case of continuous driving at a locally-resonant frequency. The sweet spot seems to be around $m = 20$, more or less the same point where resonance becomes visible in Figure 5.3. Admittedly, giant pulsations are typically closer to 10 mHz than 22 mHz. It seems likely that qualitatively similar results would be encountered if the driving were moved to an L -shell with a bounce time of 10 mHz.

Giant pulsations are seen at very large m , though not on the ground[95], due to damping by the ionosphere.

Giant pulsations are most common on the dayside (particularly the morningside), during geomagnetically quiet times. Giant pulsation ground signatures are noted for their predisposition towards east-west polarization.

In Figure 5.5, the strongest east-west ground signatures is obtained on the geomagnetically quiet dayside, at m of 16 and 32.

This seems to be a giant pulsation "sweet spot": the poloidal mode becomes stronger as m increases, but the ionospheric damping also increases.

5.3.1 Ground Signatures

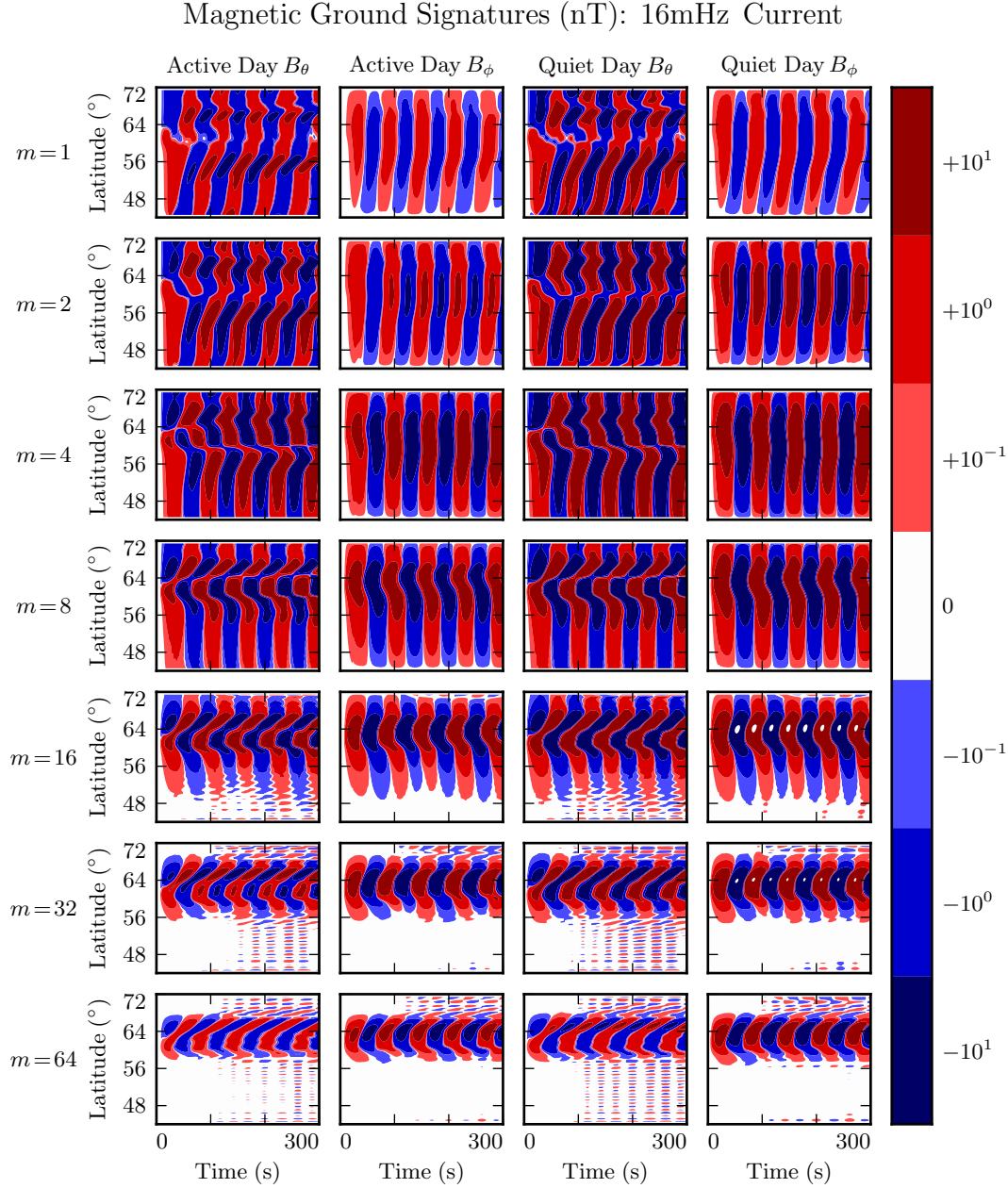


Figure 5.5: The east-west component of magnetic ground signatures is peaked on the geomagnetically quiet dayside, at modenumbers around 16 to 32. This coincides nicely with observations of giant pulsations.⁶⁶ Like the east-west component, the north-south ground signature is strongest on the quiet dayside; however, unlike the east-west component, the north-south component is weak when the modenumber is large.

Giant pulsations are monochromatic, and can be accompanied by “multiharmonic toroidal waves”[94]. Per Section 5.2, this is about what would be expected from a mishmash of poloidal driving. Poloidal modes of all frequencies rotate into the toroidal mode; resonant poloidal modes resonate; non-resonant poloidal modes become evanescent.

Giant pulsations often drift azimuthally. This model can’t resolve azimuthal drift directly, of course, but can fake it by looking at complex phase. There has been some indication (not shown) of complex phase rotation in ground magnetic fields. However, at the boundary, it’s difficult to disentangle which values are imaginary to indicate an azimuthal offset, and which are imaginary because of Hall coupling. Investigation is ongoing.

Chapter 6

Comparison to Van Allen Probes

TODO: Do we need to acknowledge that a moving spacecraft might have these fields shifted per $\underline{E} + \underline{U} \times \underline{B} = 0$?

TODO: I have met a handful of times with John (Wygant) to discuss how to get some RBSP data into this dissertation.

TODO: John has recently become interested in the long (26 d or so) cycle in the size of the plasmapause.

TODO: Lei recently compiled a list of several hundred Pc4 events seen by RBSP[13]. He binned them by plasmapause location, noting that there were a significant number of events in the entire interval $4 \lesssim L \lesssim 6$. However, he was just writing about occurrence rate, so he didn't delve into how the large-plasmasphere Pc4s were different from the small-plasmasphere ones.

TODO: I'll bet I can find a pattern or two in Pc4 behavior based on plasmapause location. It'll be interesting to see if the model exhibits the same pattern as the plasmapause location is adjusted.

TODO: I emailed Lei about this earlier this week. He sent over his event list.

TODO: Sheng has agreed to show me how to access RBSP data.

TODO: There is some concern about the rules attached to funding. Apparently NASA

fundees aren't allowed to be involved in two-person collaborations with international scientists, or something? We'll have to get that figured out.

Chapter 7

Conclusion

7.1 Summary of Results

TODO: Write this.

7.2 Future Work

Arbitrary deformation of grid. Get $\hat{e}_i = \frac{\partial}{\partial u^i} \underline{x}$, then $g_{ij} = \hat{e}_i \cdot \hat{e}_j$, then invert the metric tensor for contravariant components.

MPI. Some benchmarks with time to compute vs time to broadcast. At what problem scale does additional parallelization make sense?

Driving based on events? Wouldn't be that hard.

Test particles? Seems silly. Watching something drift-bounce resonate will require making assumptions about what's going on on the other face of the planet.

Conductivity affected by precipitation/current?

References

- [1] B. J. Anderson. An overview of spacecraft observations of 10s to 600s period magnetic pulsations in Earth’s magnetosphere. In M. J. Engebretson, K. Takahashi, and M. Scholer, editors, *Solar Wind Sources of Magnetospheric Ultra-Low-Frequency Waves*, volume 81 of *Geophys. Monogr.*, pages 25–43. American Geophysical Union, Washington, DC, 1994.
- [2] B. J. Anderson, M. J. Engebretson, S. P. Rounds, L. J. Zanetti, and T. A. Potemra. A statistical study of Pc 3-5 pulsations observed by the AMPTE/CCE magnetic fields experiment, 1. occurrence distributions. *J. Geophys. Res.*, 95(A7):10495, 1990.
- [3] C. W. Arthur and R. L. McPherron. The statistical character of Pc 4 magnetic pulsations at synchronous orbit. *J. Geophys. Res.*, 86(A3):1325, 1981.
- [4] K. Birkeland. Expédition norvégienne de 1899-1900 pour l’étude des aurores boréales. *Mat. Naturvidensk. Kl.*, KI(I), 1901.
- [5] J. P. Boris. A physically motivated solution of the Alfvén problem. *NRL Memorandum Report*, 2167, 1970.
- [6] A. Brekke, T. Feder, and S. Berger. Pc4 giant pulsations recorded in Tromsø, 1929-1985. *Journal of Atmospheric and Terrestrial Physics*, 49(10):1027–1032, 1987.
- [7] A. A. Chan, M. Xia, and L. Chen. Anisotropic alfvén-ballooning modes in Earth’s magnetosphere. *J. Geophys. Res. Space Physics*, 99(A9):17351–17366, 1994.

- [8] L. Chen and A. Hasegawa. A theory of long-period magnetic pulsations: 1. steady state excitation of field line resonance. *J. Geophys. Res.*, 79(7):1024–1032, 1974.
- [9] L. Chen and A. Hasegawa. Kinetic theory of geomagnetic pulsations: 1. internal excitations by energetic particles. *J. Geophys. Res.*, 96(A2):1503, 1991.
- [10] C. Z. Cheng and Q. Qian. Theory of ballooning-mirror instabilities for anisotropic pressure plasmas in the magnetosphere. *J. Geophys. Res.*, 99(A6):11193, 1994.
- [11] W. D. Cummings, R. J. O’Sullivan, and P. J. Coleman. Standing Alfvén waves in the magnetosphere. *J. Geophys. Res.*, 74(3):778–793, 1969.
- [12] L. Dai. Collisionless magnetic reconnection via Alfvén eigenmodes. *Phys. Rev. Lett.*, 102(24), 2009.
- [13] L. Dai, K. Takahashi, R. Lysak, C. Wang, J. R. Wygant, C. Kletzing, J. Bonnell, C. A. Cattell, C. W. Smith, R. J. MacDowall, S. Thaller, A. Breneman, X. Tang, X. Tao, and L. Chen. Storm time occurrence and spatial distribution of Pc4 poloidal ULF waves in the inner magnetosphere: A Van Allen Probes statistical study. *J. Geophys. Res. Space Physics*, 120:4748–4762, 2015.
- [14] L. Dai, K. Takahashi, J. R. Wygant, L. Chen, J. Bonnell, C. A. Cattell, S. Thaller, C. Kletzing, C. W. Smith, R. J. MacDowall, D. N. Baker, J. B. Blake, J. Fennell, S. Claudepierre, H. O. Funsten, G. D. Reeves, and H. E. Spence. Excitation of poloidal standing Alfvén waves through drift resonance wave-particle interaction. *Geophys. Res. Lett.*, 40:4127–4132, 2013.
- [15] A. W. Degeling, R. Rankin, and Q.-G. Zong. Modeling radiation belt electron acceleration by ULF fast mode waves, launched by solar wind dynamic pressure fluctuations. *J. Geophys. Res. Space Physics*, 119(11):8916–8928, 2014.
- [16] R. E. Denton, M. F. Thomsen, K. Takahashi, R. R. Anderson, and H. J. Singer. Solar cycle dependence of bulk ion composition at geosynchronous orbit. *J. Geophys. Res.*, 116(A3), 2011.
- [17] W. D. D’haeseleer, W. N. G. H. J. D. Callen, and J. L. Shohet. *Flux Coordinates and Magnetic Field Structure*. Springer-Verlag, New York, 1991.

- [18] D. Q. Ding, R. E. Denton, M. K. Hudson, and R. L. Lysak. An MHD simulation study of the poloidal mode field line resonance in the Earth's dipole magnetosphere. *J. Geophys. Res.*, 100:63–77, 1995.
- [19] J. W. Dungey. The attenuation of Alfvén waves. *J. Geophys. Res.*, 59(3):323–328, 1954.
- [20] A. Einstein. Die grundlage der allgemeinen relativitätstheorie. *Ann. Phys.*, 354:769–822, 1916.
- [21] S. R. Elkington. Resonant acceleration and diffusion of outer zone electrons in an asymmetric geomagnetic field. *J. Geophys. Res.*, 108(A3), 2003.
- [22] S. R. Elkington, M. K. Hudson, and A. A. Chan. Acceleration of relativistic electrons via drift-resonant interaction with toroidal-mode Pc-5 ULF oscillations. *Geophys. Res. Lett.*, 26(21):3273–3276, 1999.
- [23] M. J. Engebretson, D. L. Murr, K. N. Erickson, R. J. Strangeway, D. M. Klumpar, S. A. Fuselier, L. J. Zanetti, and T. A. Potemra. The spatial extent of radial magnetic pulsation events observed in the dayside near synchronous orbit. *J. Geophys. Res.*, 97(A9):13741, 1992.
- [24] M. J. Engebretson, L. J. Zanetti, T. A. Potemra, W. Baumjohann, H. Lühr, and M. H. Acuna. Simultaneous observation of Pc 34 pulsations in the solar wind and in the Earth's magnetosphere. *J. Geophys. Res. Space Physics*, 92:10053–10062, 1987.
- [25] M. J. Engebretson, L. J. Zanetti, T. A. Potemra, D. M. Klumpar, R. J. Strangeway, and M. H. Acuña. Observations of intense ULF pulsation activity near the geomagnetic equator during quiet times. *J. Geophys. Res.*, 93(A11):12795, 1988.
- [26] P. T. I. Eriksson, L. G. Blomberg, A. D. M. Walker, and K.-H. Glassmeier. Poloidal ULF oscillations in the dayside magnetosphere: a Cluster study. *Ann. Geophys.*, 23(7):2679–2686, 2005.
- [27] S. Fujita and T. Tamao. Duct propagation of hydromagnetic waves in the upper ionosphere, 1, electromagnetic field disturbances in high latitudes associated with localized incidence of a shear Alfvén wave. *J. Geophys. Res.*, 93(A12):14665, 1988.

- [28] K.-H. Glassmeier. Magnetometer array observations of a giant pulsation event. *J. Geophys.*, 48:127–138, 1980.
- [29] K.-H. Glassmeier. On the influence of ionospheres with non-uniform conductivity distribution on hydromagnetic waves. *J. Geophys.*, 54(2):125–137, 1984.
- [30] K.-H. Glassmeier, S. Buchert, U. Motschmann, A. Korth, and A. Pedersen. Concerning the generation of geomagnetic giant pulsations by drift-bounce resonance ring current instabilities. *Ann. Geophysicae*, 17:338–350, 1999.
- [31] K.-H. Glassmeier, D. Klimushkin, C. Othmer, and P. Mager. ULF waves at mercury: Earth, the giants, and their little brother compared. *Advances in Space Research*, 33(11):1875–1883, 2004.
- [32] K.-H. Glassmeier and M. Stellmacher. Concerning the local time asymmetry of Pc5 wave power at the ground and field line resonance widths. *J. Geophys. Res.*, 105(A8):18847–18855, 2000.
- [33] C. A. Green. Observations of Pg pulsations in the northern auroral zone and at lower latitude conjugate regions. *Planetary and Space Science*, 27(1):63–77, 1979.
- [34] C. A. Green. Giant pulsations in the plasmasphere. *Planetary and Space Science*, 33(10):1155–1168, 1985.
- [35] C. Greifinger and P. S. Greifinger. Theory of hydromagnetic propagation in the ionospheric waveguide. *J. Geophys. Res.*, 73(23):7473–7490, 1968.
- [36] G. Haerendel, W. Baumjohann, E. Georgescu, R. Nakamura, L. M. Kistler, B. Klecker, H. Kucharek, A. Vaivads, T. Mukai, and S. Kokubun. High-beta plasma blobs in the morningside plasma sheet. *Ann. Geophys.*, 17(12):1592–1601, 1999.
- [37] B. C. Hall. *Lie Groups, Lie Algebras, and Representations*. Graduate Texts in Mathematics. Springer, New York, second edition, 2015.
- [38] Y. X. Hao, Q.-G. Zong, Y. F. Wang, X.-Z. Zhou, H. Zhang, S. Y. Fu, Z. Y. Pu, H. E. Spence, J. B. Blake, J. Bonnell, J. R. Wygant, and C. A. Kletzing. Interactions of energetic electrons with ULF waves triggered by interplanetary

- shock: Van allen probes observations in the magnetotail. *J. Geophys. Res. Space Physics*, 119(10):8262–8273, 2014.
- [39] A. Hasegawa. Drift-wave instability at the plasmapause. *J. Geophys. Res.*, 76(22):5361–5364, 1971.
 - [40] O. Hillebrand, J. Muench, and R. L. McPherron. Ground-satellite correlative study of a giant pulsation event. *Journal of Geophysics Zeitschrift Geophysik*, 51:129–140, 1982.
 - [41] W. J. Hughes. The effect of the atmosphere and ionosphere on long period magnetospheric micropulsations. *Planet. Space Sci.*, 22:1157–1172, 1974.
 - [42] W. J. Hughes. Magnetospheric ULF waves: A tutorial with a historical perspective. In M. J. Engebretson, K. Takahashi, and M. Scholer, editors, *Solar Wind Sources of Magnetospheric Ultra-Low-Frequency Waves*, volume 81 of *Geophys. Monogr.*, pages 1–12. American Geophysical Union, Washington, DC, 1994.
 - [43] W. J. Hughes and D. J. Southwood. The screening of micropulsation signals by the atmosphere and ionosphere. *J. Geophys. Res.*, 81(19):3234–3240, 1976.
 - [44] W. J. Hughes, D. J. Southwood, B. Mauk, R. L. McPherron, and J. N. Barfield. Alfvén waves generated by an inverted plasma energy distribution. *Nature*, 275(5675):43–45, 1978.
 - [45] J. A. Jacobs, Y. Kato, S. Matsushita, and V. A. Troitskaya. Classification of geomagnetic micropulsations. *J. Geophys. Res.*, 69(1):180–181, 1964.
 - [46] A. N. Jaynes, M. R. Lessard, K. Takahashi, A. F. Ali, D. M. Malaspina, R. G. Michell, E. L. Spanswick, D. N. Baker, J. B. Blake, C. Cully, E. F. Donovan, C. A. Kletzing, G. D. Reeves, M. Samara, H. E. Spence, and J. R. Wygant. Correlated Pc45 ULF waves, whistler-mode chorus, and pulsating aurora observed by the Van Allen Probes and ground-based systems. *J. Geophys. Res. Space Physics*, 120:87498761, 2015.
 - [47] Y. Kato and T. Tsutomu. Hydromagnetic oscillations in a conducting medium with hall conduct-ivity under the uniform magnetic field. *Science reports of the Tohoku University. Ser. 5, Geophysics*, 7(3):147–164, 1956.

- [48] M. C. Kelley. *The Earth's Ionosphere*. Academic Press, San Diego, second edition, 1989.
- [49] R. L. Kessel. Solar wind excitation of pc5 fluctuations in the magnetosphere and on the ground. *J. Geophys. Res.*, 113(A4), 2008.
- [50] M. G. Kivelson. Ulf waves from the ionosphere to the outer planets. In K. Takahashi, P. J. Chi, R. E. Denton, and R. L. Lysak, editors, *Magnetospheric ULF Waves: Synthesis and New Directions*, volume 169 of *Geophys. Monogr.*, pages 11–30. American Geophysical Union, Washington, DC, 2006.
- [51] D. Y. Klimushkin. Resonators for hydromagnetic waves in the magnetosphere. *J. Geophys. Res.*, 103(A2):2369–2375, 1998.
- [52] D. Y. Klimushkin, P. N. Mager, and K.-H. Glassmeier. Toroidal and poloidal Alfvén waves with arbitrary azimuthal wavenumbers in a finite pressure plasma in the earth’s magnetosphere. *Annales Geophysicae*, 22(1):267–287, 2004.
- [53] S. Kokubun. Observations of Pc pulsations in the magnetosphere: Satellite-ground correlation. *J. Geomagn. Geoelec*, 32(Supplement2):SII17–SII39, 1980.
- [54] S. Kokubun, K. N. Erickson, T. A. Fritz, and R. L. McPherron. Local time asymmetry of Pc 4-5 pulsations and associated particle modulations at synchronous orbit. *J. Geophys. Res.*, 94(A6):6607–6625, 1989.
- [55] D.-H. Lee. On the generation mechanism of pi 2 pulsations in the magnetosphere. *Geophys. Res. Lett.*, 25(5):583–586, 1998.
- [56] D.-H. Lee and K. Kim. Compressional MHD waves in the magnetosphere: A new approach. *J. Geophys. Res.*, 104(A6):12379–12385, 1999.
- [57] A. S. Leonovich and V. A. Mazur. Structure of magnetosonic eigenoscillations of an axisymmetric magnetosphere. *J. Geophys. Res.*, 105(A12):27707–27715, 2000.
- [58] W. Liu, J. B. Cao, X. Li, T. E. Sarris, Q.-G. Zong, M. Hartinger, K. Takahashi, H. Zhang, Q. Q. Shi, and V. Angelopoulos. Poloidal ULF wave observed in the plasmasphere boundary layer. *J. Geophys. Res. Space Physics*, 118(7):4298–4307, 2013.

- [59] W. Liu, T. E. Sarris, X. Li, S. R. Elkington, R. Ergun, V. Angelopoulos, J. Bonnell, and K. H. Glassmeier. Electric and magnetic field observations of Pc4 and Pc5 pulsations in the inner magnetosphere: A statistical study. *J. Geophys. Res.*, 114(A12), 2009.
- [60] W. Liu, T. E. Sarris, X. Li, Q.-G. Zong, R. Ergun, V. Angelopoulos, and K. H. Glassmeier. Spatial structure and temporal evolution of a dayside poloidal ULF wave event. *Geophys. Res. Lett.*, 38(19), 2011.
- [61] R. L. Lysak. Magnetosphere-ionosphere coupling by Alfvén waves at midlatitudes. *J. Geophys. Res.*, 109, 2004.
- [62] R. L. Lysak and D. hun Lee. Response of the dipole magnetosphere to pressure pulses. *Geophys. Res. Lett.*, 19(9):937–940, 1992.
- [63] R. L. Lysak and Y. Song. A three-dimensional model of the propagation of Alfvén waves through the auroral ionosphere: first results. *Adv. Space Res.*, 28:813–822, 2001.
- [64] R. L. Lysak and Y. Song. Development of parallel electric fields at the plasma sheet boundary layer. *J. Geophys. Res. Space Physics*, 116, 2011.
- [65] R. L. Lysak, C. L. Waters, and M. D. Sciffer. Modeling of the ionospheric Alfvén resonator in dipolar geometry. *J. Geophys. Res. Space Physics*, 118, 2013.
- [66] R. L. Lysak and A. Yoshikawa. Resonant cavities and waveguides in the ionosphere and atmosphere. In K. Takahashi, P. J. Chi, R. E. Denton, and R. L. Lysak, editors, *Magentospheric ULF Waves: Synthesis and New Directions*, volume 169 of *Geophys. Monogr.*, page 289. American Geophysical Union, Washington, DC, 2006.
- [67] P. N. Mager and D. Y. Klimushkin. Giant pulsations as modes of a transverse Alfvénic resonator on the plasmapause. *Earth, Planets and Space*, 65(5):397–409, 2013.
- [68] I. R. Mann, E. A. Lee, S. G. Claudepierre, J. F. Fennell, A. Degeling, I. J. Rae, D. N. Baker, G. D. Reeves, H. E. Spence, L. G. Ozeke, R. Rankin, D. K. Milling, A. Kale, R. H. W. Friedel, and F. Honary. Discovery of the action of a geophysical

- synchrotron in the Earth’s Van Allen radiation belts. *Nature Communications*, 4, 2013.
- [69] I. R. Mann and A. N. Wright. Finite lifetimes of ideal poloidal Alfvén waves. *J. Geophys. Res.*, 100:23677–23686, 1995.
 - [70] I. R. Mann, A. N. Wright, and A. W. Hood. Multiple-timescales analysis of ideal poloidal Alfvén waves. *J. Geophys. Res.*, 102(A2):2381–2390, 1997.
 - [71] T. Motoba, K. Takahashi, J. V. Rodriguez, and C. T. Russell. Giant pulsations on the afternoonside: Geostationary satellite and ground observations. *J. Geophys. Res. Space Physics*, 120:8350–8367, 2015.
 - [72] NASA. Coordinated data analysis (workshop) web.
 - [73] J. V. Olson and G. Rostoker. Longitudinal phase variations of Pc 4-5 micropulsations. *J. Geophys. Res. Space Physics*, 83(A6):2481–2488, 1978.
 - [74] L. G. Ozeke and I. R. Mann. Modeling the properties of high-m Alfvén waves driven by the drift-bounce resonance mechanism. *J. Geophys. Res.*, 106(A8):15583–15597, 2001.
 - [75] L. G. Ozeke and I. R. Mann. Energization of radiation belt electrons by ring current ion driven ULF waves. *J. Geophys. Res.*, 113(A2), 2008.
 - [76] L. G. Ozeke, I. R. Mann, K. R. Murphy, I. J. Rae, D. K. Milling, S. R. Elkington, A. A. Chan, and H. J. Singer. ULF wave derived radiation belt radial diffusion coefficients. *J. Geophys. Res.*, 117(A4), 2012.
 - [77] G. Paschmann, S. Haaland, and R. Treumann, editors. *Auroral Plasma Physics*, volume 15. Kluwer Academic Publishers, 2003.
 - [78] E. M. Poulter, W. Allan, E. Nielsen, and K.-H. Glassmeier. Stare radar observations of a PG pulsation. *J. Geophys. Res.*, 88(A7):5668, 1983.
 - [79] J. A. Proehl, W. Lotko, I. Kouznetsov, and S. D. Geimer. Ultralow-frequency magnetohydrodynamics in boundary-constrained geomagnetic flux coordinates. *J. Geophys. Res.*, 107(A9):1225, 2002.

- [80] H. R. Radoski. Highly asymmetric MHD resonances: the guided poloidal mode. *J. Geophys. Res.*, 72(15), 1967.
- [81] H. R. Radoski. A note on oscillating field lines. *J. Geophys. Res.*, 72(1), 1967.
- [82] H. R. Radoski. A theory of latitude dependent geomagnetic micropulsations: The asymptotic fields. *J. Geophys. Res.*, 79, 1974.
- [83] K. Rönnmark and M. Hamrin. Auroral electron acceleration by Alfvén waves and electrostatic fields. *J. Geophys. Res.*, 105:25333–25344, 2000.
- [84] G. Rostoker, H.-L. Lam, and J. V. Olson. PC 4 giant pulsations in the morning sector. *J. Geophys. Res.*, 84(A9):5153, 1979.
- [85] C. T. Russell, J. G. Luhmann, T. J. Odera, and W. F. Stuart. The rate of occurrence of dayside Pc 3,4 pulsations: The L-value dependence of the IMF cone angle effect. *Geophys. Res. Lett.*, 10(8):663–666, 1983.
- [86] D. G. Sibeck, G. Korotova, D. L. Turner, V. Angelopoulos, K.-H. Glaßmeier, and J. P. McFadden. Frequency doubling and field-aligned ion streaming in a long-period poloidal pulsation. *J. Geophys. Res.*, 117(A11), 2012.
- [87] H. J. Singer, W. J. Hughes, and C. T. Russell. Standing hydromagnetic waves observed by ISEE 1 and 2: Radial extent and harmonic. *J. Geophys. Res.*, 87(A5):3519, 1982.
- [88] D. J. Southwood. Some features of field line resonances in the magnetosphere. *Planetary and Space Science*, 22(3):483–491, 1974.
- [89] D. J. Southwood. A general approach to low-frequency instability in the ring current plasma. *J. Geophys. Res.*, 81(19):3340–3348, 1976.
- [90] K. Takahashi, D. Berube, D.-H. Lee, J. Goldstein, H. J. Singer, F. Honary, and M. B. Moldwin. Possible evidence of virtual resonance in the dayside magnetosphere. *J. Geophys. Res.*, 114(A5), 2009.
- [91] K. Takahashi, J. Bonnell, K.-H. Glassmeier, V. Angelopoulos, H. J. Singer, P. J. Chi, R. E. Denton, Y. Nishimura, D.-H. Lee, M. Nosé, and W. Liu. Multipoint

- observation of fast mode waves trapped in the dayside plasmasphere. *J. Geophys. Res.*, 115(A12), 2010.
- [92] K. Takahashi, R. E. Denton, W. Kurth, C. Kletzing, J. Wygant, J. Bonnell, L. Dai, K. Min, C. W. Smith, and R. MacDowall. Externally driven plasmaspheric ULF waves observed by the Van Allen Probes. *J. Geophys. Res. Space Physics*, 120(1):526–552, 2015.
- [93] K. Takahashi, J. F. Fennell, E. Amata, and P. R. Higbie. Field-aligned structure of the storm time Pc 5 wave of november 14–15, 1979. *J. Geophys. Res.*, 92(A6):5857, 1987.
- [94] K. Takahashi, K.-H. Glassmeier, V. Angelopoulos, J. Bonnell, Y. Nishimura, H. J. Singer, and C. T. Russell. Multisatellite observations of a giant pulsation event. *J. Geophys. Res.*, 116:A11223, 2011.
- [95] K. Takahashi, M. D. Hartinger, V. Angelopoulos, K.-H. Glassmeier, and H. J. Singer. Multispacecraft observations of fundamental poloidal waves without ground magnetic signatures. *J. Geophys. Res. Space Physics*, 118:4319–4334, 2013.
- [96] K. Takahashi, R. W. McEntire, A. T. Y. Lui, and T. A. Potemra. Ion flux oscillations associated with a radially polarized transverse Pc 5 magnetic pulsation. *J. Geophys. Res.*, 95(A4):3717, 1990.
- [97] K. Takahashi and R. L. McPherron. Standing hydromagnetic oscillations in the magnetosphere. *Planetary and Space Science*, 32:1343–1359, 1984.
- [98] K. Takahashi, N. Sato, J. Warnecke, H. Lühr, H. E. Spence, and Y. Tonegawa. On the standing wave mode of giant pulsations. *J. Geophys. Res. Space Physics*, 97(A7):10717–10732, 1992.
- [99] T. Tamao. Transmission and coupling resonance of hydromagnetic disturbances in the non-uniform Earth’s magnetosphere. *Sci. Rept. Tohoku Univ.*, 17(2):43, 1965.
- [100] S. M. Thompson and M. G. Kivelson. New evidence for the origin of giant pulsations. *J. Geophys. Res.*, 106(A10):21237–21253, 2001.

- [101] W. Tu, S. R. Elkington, X. Li, W. Liu, and J. Bonnell. Quantifying radial diffusion coefficients of radiation belt electrons based on global MHD simulation and spacecraft measurements. *J. Geophys. Res.*, 117(A10), 2012.
- [102] A. Vaivads, W. Baumjohann, G. Haerendel, R. Nakamura, H. Kucharek, B. Klecker, M. R. Lessard, L. M. Kistler, T. Mukai, and A. Nishida. Compressional Pc5 type pulsations in the morningside plasma sheet. *Ann. Geophys.*, 19(3):311–320, 2001.
- [103] C. L. Waters, R. L. Lysak, and M. D. Sciffer. On the coupling of fast and shear Alfvén wave modes by the ionospheric Hall conductance. *Earth Planets Space*, 65:385–396, 2013.
- [104] C. L. Waters and M. D. Sciffer. Field line resonant frequencies and ionospheric conductance: Results from a 2-d MHD model. *J. Geophys. Res.*, 113(A5), 2008.
- [105] J. R. Woodroffe and R. L. Lysak. Ultra-low frequency wave coupling in the ionospheric Alfvén resonator: Characteristics and implications for the interpretation of ground magnetic fields. *J. Geophys. Res.*, 117:A03223, 2012.
- [106] D. M. Wright and T. K. Yeoman. High-latitude HF doppler observations of ULF waves: 2. waves with small spatial scale sizes. *Ann. Geophys.*, 17(7):868–876, 1999.
- [107] B. Yang, Q.-G. Zong, Y. F. Wang, S. Y. Fu, P. Song, H. S. Fu, A. Korth, T. Tian, and H. Reme. Cluster observations of simultaneous resonant interactions of ULF waves with energetic electrons and thermal ion species in the inner magnetosphere. *J. Geophys. Res.*, 115(A2), 2010.
- [108] T. K. Yeoman and D. M. Wright. ULF waves with drift resonance and drift-bounce resonance energy sources as observed in artificially-induced HF radar backscatter. *Ann. Geophys.*, 19(2):159–170, 2001.
- [109] Q.-G. Zong, X.-Z. Zhou, X. Li, P. Song, S. Y. Fu, D. N. Baker, Z. Y. Pu, T. A. Fritz, P. Daly, A. Balogh, and H. Réme. Ultralow frequency modulation of energetic particles in the dayside magnetosphere. *Geophys. Res. Lett.*, 34(12), 2007.

- [110] Q.-G. Zong, X.-Z. Zhou, Y. F. Wang, X. Li, P. Song, D. N. Baker, T. A. Fritz, P. W. Daly, M. Dunlop, and A. Pedersen. Energetic electron response to ULF waves induced by interplanetary shocks in the outer radiation belt. *J. Geophys. Res.*, 114(A10), 2009.

Appendix A

Differential Geometry

TODO: Not sure that a glossary or list of acronyms will be necessary, but here are the examples from the template.

A.1 Glossary

- **Cosmic-Ray Muon (CR μ)** – A muon coming from the abundant energetic particles originating outside of the Earth's atmosphere.

A.2 Acronyms

Table A.1: Acronyms

Acronym	Meaning
CR μ	Cosmic-Ray Muon